Navier-Stokes characteristic boundary conditions for high-enthalpy compressible flows in thermochemical non-equilibrium ☆

Christopher Williams [a,*], Mario Di Renzo [a], Javier Urzay [b], Parviz Moin [a]

[a] *Center for Turbulence Research, Stanford University, CA 94305, United States of America*
[b] *US Space Force at Rocket Propulsion Division, Air Force Research Laboratory, Edwards AFB, CA 93526, United States of America*

ARTICLE INFO

ABSTRACT

This fundamental study presents Navier-Stokes characteristic boundary conditions (NSCBCs) for high-enthalpy hypersonic flows in thermochemical non-equilibrium. In particular, the relevant locally one-dimensional inviscid (LODI) relations are derived within a two-temperature framework for high-enthalpy hypersonic flows undergoing finite-rate thermochemical processes, including air dissociation and vibrational relaxation. Using these LODI relations, a set of NSCBCs are proposed and later demonstrated in canonical test cases, including the interaction of homogeneous isotropic turbulence with a shock wave subject to high-enthalpy thermochemical non-equilibrium effects.

1. Introduction

The presence of strong shock waves, together with kinetic energy dissipation in boundary layers, activates a number of high-enthalpy effects in hypersonic flows, including both chemical dissociation and vibrational excitation. As both chemical reactions and thermal relaxation proceed at finite rates, on time scales often comparable to that of advection, hypersonic flows are largely characterized as in a state of thermochemical non-equilibrium [1].

In hypersonic flows, thermochemical non-equilibrium is most significant in the vicinity of shock waves, across which preferential excitation of rotational and translational internal energy modes activates vibrational relaxation. Accurate characterization of internal energy modes is necessary not only for determining fluxes of internal energy, but also for predicting the rates of chemical processes, as the extent of vibrational excitation influences dissociation rates via vibration-dissociation coupling [2–6]. Owing to the significant dissociation energies of the different molecular constituents of air at high temperatures, finite-rate vibrational relaxation can strongly impact the thermal field via its coupling with reaction rates, inhibiting the exchange between sensible and chemical energy. Likewise, vibrational non-equilibrium also affects the hydrodynamic field in hypersonic flows via the coupling of pressure and temperature through the equation of state.

Fundamental problems in hypersonic aerothermodynamics often require spatio-temporal resolution of unsteady phenomena associated with shock waves and turbulent eddies [7–11]. For high-enthalpy flows, the interactions between compressible turbulence and thermochemical processes were originally characterized in the context of temporally evolving boundary layers by Duan & Martin

[12], with subsequent work by Di Renzo & Urzay [13] addressing the impact of chemical nonequilibrium on a spatially-evolving transitional/turbulent boundary layer of air in the stratosphere at Mach 10 over a cold wall. Most recently, Passiatore et al. [14] considered the coupling between turbulent motion and vibrational relaxation in a high-Mach turbulent boundary layer. Nevertheless, the mutual interactions between shock waves, turbulence, and nonequilibrium thermochemical processes remain poorly characterized overall, particularly in shock-dominated flows. As such, there remains a need for more general boundary conditions that can be used with confidence in Direct Numerical Simulation (DNS) and Large Eddy Simulation (LES) frameworks for high-enthalpy hypersonic flows.

The present study introduces appropriately modified characteristics-based boundary conditions that account for high-temperature gasdynamic phenomena. While Thompson [15,16] first introduced characteristics-based boundary conditions for hyperbolic partial differential equations, Poinsot and Lele [17] later extended characteristic boundary conditions for the compressible Navier-Stokes equations. Subsequent work by Lodato et al. [18] extended the analysis to three dimensions in order to account for the oblique propagation of waves relative to the outflow boundary. Effects of chemical reactions in compressible flows with high-pressure equations of state were considered by Baum et al. [19], Okong'o & Bellan [20], and Ju et al. [21], with these studies being limited to thermal-equilibrium conditions. In this study, the locally one-dimensional Navier-Stokes characteristic boundary conditions (NSCBCs) of Okong'o & Bellan are extended to account for thermochemical non-equilibrium processes arising in hypersonic flows at high enthalpies, including vibration-dissociation coupling and vibrational relaxation. Whereas fully three-dimensional boundary conditions have largely proven crucial for the computational analysis of combustion [22,23], the locally one-dimensional treatment developed herein for non-equilibrium hypersonic flows proves sufficient for the unsteady flows analyzed. Extensions to three-dimensional formulations of the boundary conditions using methods similar to those in Ref. [18], which may be necessary for more complex flow configurations, are therefore deferred to future work.

The remainder of this manuscript is organized as follows. Section 2 presents the relevant set of conservation equations together with the corresponding thermodynamics, transport, and kinetics for two-temperature high-enthalpy hypersonic turbulent flows. Section 3 derives the corresponding locally one-dimensional inviscid (LODI) relations. Section 4 presents the set of NSCBCs associated with the LODI relations. Section 5 applies the characteristic boundary conditions derived in the present study to a set of canonical test cases subject to thermochemical non-equilibrium effects, which include the interaction of a shock wave with homogeneous isotropic turbulence. Lastly, Section 6 provides concluding remarks.

2. Formulation of the conservation equations

One approach for modeling the effect of finite-rate relaxation of internal energy modes in hypersonic flows is the multi-temperature formulation of the conservation equations, for which each energy mode is characterized by a Boltzmann distribution with a distinct temperature [1,3,24]. Owing to the fast relaxation of rotational energy modes, most approaches for modeling and simulation of hypersonic flows utilize only two temperatures in the formulation. Specifically, the rotational and translational energies are both characterized by a common temperature T, while the vibrational and electronic energies are likewise assumed to be in equilibrium at a separate temperature T_{ve} [25,26].

It should be emphasized that the NSCBCs provided in this study are independent of many aspects of the formulation of the conservation equations presented below. In particular, whereas this Section outlines Park's standard two-temperature formulation [1], which is later integrated numerically in Section 5 for selected cases, the derivation of the LODI relations presented in Section 3 is general and independent of the thermophysical, transport, and chemical-kinetic models. For instance, the proposed NSCBCs can be used in conjunction with other descriptions for the coupling between vibrational excitation and dissociation, including the modified Marrone-Treanor model [5].

In the two-temperature formulation of multi-component hypersonic flows, the species partial density conservation equations can be expressed as

$$\frac{\partial(\rho Y_i)}{\partial t} + \nabla\cdot(\rho Y_i \mathbf{u}) = -\nabla\cdot\left(\rho Y_i \boldsymbol{V}_i\right) + \dot{w}_i \qquad i = 1,...,N_s, \tag{1}$$

where Y_i is the mass fraction for species i, ρ is the mixture density, $\mathbf{u} = [u\ v\ w]^T$ is the mass-averaged velocity of the mixture, $\boldsymbol{V}_i$ is the diffusion velocity for species i, and $\dot{w}_i$ is the net rate of mass production of species i per unit volume. The diffusion velocity for each species is computed as [27–29]

$$\boldsymbol{V}_i = -D_i \nabla\ln X_i + \sum_{j=1}^{N_s} Y_j D_j \nabla\ln X_i, \tag{2}$$

where D_i and X_i are taken to be, respectively, the mixture-averaged mass diffusivity and molar fraction of species i.

The chemical mechanism for air dissociation considered in this study is given by the reactions

$$N_2 + M \rightleftharpoons 2N + M, \tag{R1}$$

$$O_2 + M \rightleftharpoons 2O + M, \tag{R2}$$

$$NO + M \rightleftharpoons N + O + M, \tag{R3}$$

$$N_2 + O \rightleftharpoons NO + N, \tag{R4}$$

$$NO + O \rightleftharpoons O_2 + N. \tag{R5}$$

In this mechanism, (R1)-(R3) represent dissociation (forward) or recombination (backward) reactions for bimolecular species, whereas (R4) and (R5) are shuffle reactions responsible for the thermal production of nitric oxide. The symbol M represents any collider present in the mixture. As a result, the number of species in the expressions above is $N_s = 5$, whereas the number of reactions is $N_r = 17$ accounting for all colliders. In this notation, the chemical production term in Eq. (1) can be expressed as

$$\dot{w}_i = \mathcal{M}_i \sum_{j=R1}^{R5} \left(\nu''_{ij} - \nu'_{ij} \right) \left[k_{f,j} \prod_{k=1}^{N_s} \left(\frac{\rho Y_k}{\mathcal{M}_k} \right)^{\nu'_{kj}} - k_{b,j} \prod_{k=1}^{N_s} \left(\frac{\rho Y_k}{\mathcal{M}_k} \right)^{\nu''_{kj}} \right], \tag{3}$$

where $\mathcal{M}_i$ is the molecular weight of species i, and ν'_{kj} and ν''_{kj} are the stoichiometric coefficients of species k in reaction j in the forward and reverse directions, respectively. The rate constants for the dissociation steps are given by [1]

$$k_{f,j} = A_j \left(T T_{ve} \right)^{m_j/2} \exp \left(-\frac{E_{a,j}}{R^0 \sqrt{T T_{ve}}} \right), \qquad j = R1, R2, R3, \tag{4}$$

with R^0 being the universal gas constant. In this formulation, A_j, m_j, and $E_{a,j}$ are Arrhenius parameters that are listed in Table 1 of Ref. [30] for each reaction j and collider M. In contrast, the forward rates for the shuffle reactions (R4) and (R5) remain unaffected by thermal non-equilibrium, and are therefore evaluated at the translational-rotational temperature as [1]

$$k_{f,j} = A_j T^{m_j} \exp \left(-\frac{E_{a,j}}{R^0 T} \right), \qquad j = R4, R5, \tag{5}$$

where A_j, m_j, and $E_{a,j}$ are taken from Table 5 in Ref. [31]. The recombination (backward) rate constants are given by [1,26,32–34]

$$k_{b,j} = \frac{A_j T^{m_j}}{K_{eq,j}(T)} \exp \left(-\frac{E_{a,j}}{R^0 T} \right), \qquad j = R1, ..., R5, \tag{6}$$

where $K_{eq,j}$ is the chemical equilibrium constant for each reaction calculated using the polynomial form

$$K_{eq,j} = \exp \left(\frac{\mathcal{A}_{1,j}}{Z} + \mathcal{A}_{2,j} + \mathcal{A}_{3,j} \log Z + \mathcal{A}_{4,j} Z + \mathcal{A}_{5,j} Z^2 \right), \tag{7}$$

with $Z = 10^4/T$. The numerical values of the coefficients $\mathcal{A}_{i,j}$ are provided in Ref. [1].

The momentum conservation equation is written as

$$\frac{\partial(\rho \mathbf{u})}{\partial t} + \nabla \cdot (\rho \mathbf{u} \mathbf{u}) = -\nabla P + \nabla \cdot \overline{\overline{\tau}}, \tag{8}$$

where the pressure P is computed using the ideal-gas equation of state

$$P = \rho R^0 T / \overline{\mathcal{M}}. \tag{9}$$

In this expression, T is the translational-rotational temperature, and $\overline{\mathcal{M}} = \left[\sum_{i=1}^{N_s} Y_i/\mathcal{M}_i \right]^{-1}$ is the average molecular weight of the mixture. In accordance with Stokes' hypothesis, the viscous stress tensor is expressed as

$$\overline{\overline{\tau}} = 2\mu \overline{\overline{S}} - \frac{2\mu}{3} \left(\nabla \cdot \mathbf{u} \right) \overline{\overline{I}}, \tag{10}$$

where $\overline{\overline{S}} = \left(\nabla \boldsymbol{u} + \nabla \boldsymbol{u}^T \right)/2$ and $\overline{\overline{I}}$ are the strain-rate and identity tensors, respectively. The dynamic viscosity of the mixture, μ, is computed using Wilke's mixture rule [35], with the elementary viscosity of each component computed using the approach in Ref. [27].

The conservation equation for the specific stagnation internal energy E (including chemical energy) is

$$\frac{\partial(\rho E)}{\partial t} + \nabla \cdot (\rho E \mathbf{u}) = \nabla \cdot \left(-\mathbf{u} P + \overline{\overline{\tau}} \mathbf{u} + \lambda_{tr} \nabla T + \lambda_{ve} \nabla T_{ve} - \rho \sum_{i=1}^{N_s} Y_i \boldsymbol{V}_i h_i \right). \tag{11}$$

In this formulation, λ_{tr} is the sum of the thermal conductivity of the rotational and translational energy modes, and λ_{ve} is the combined thermal conductivity of the vibrational and electronic energy modes. While the individual thermal conductivities of each species are calculated via Eucken's relation [36], the mixture-weighted conductivities for each internal energy mode are obtained via Wilke's rule. The specific internal energy e accounts for the different energy modes as

$$e = \sum_{i=1}^{N_s} Y_i \left(e_{tr,i} + e_{v,i} + e_{e,i} + h^0_{i,f} \right), \tag{12}$$

with $h^0_{i,f}$ being the enthalpy of formation of species i at zero absolute temperature. Correspondingly, h_i is the partial specific enthalpy of species i defined as

$$h_i = \sum_{i=1}^{N_s} Y_i \left(\mathrm{R}^0 T / \mathcal{M}_i + e_{tr,i} + e_{v,i} + e_{e,i} + h_{i,f}^0 \right). \tag{13}$$

In these expressions, $e_{v,i}$, and $e_{e,i}$ are the specific internal energies of vibration and electronic excitation of species i, respectively. Similarly, $e_{tr,i}$ represents the sum of translational and rotational internal energies of species i.

The rotational and translational modes are taken to be fully excited, with the molecular species being treated as rigid rotors, namely

$$e_{tr,i} = (3/2)\mathrm{R}^0 T / \mathcal{M}_i + \mathcal{V}_i \mathrm{R}^0 T / \mathcal{M}_i. \tag{14}$$

In this notation, the prefactor $\mathcal{V}_i$ is equal to 0 and 1 for monoatomic and diatomic species, respectively. The computation of the vibrational energy is based on the treatment of molecules as quantum harmonic oscillators [36], where both the vibrational and electronic-excitation energy modes are characterized by the vibrational-electronic temperature, T_{ve}, as

$$e_{v,i} = \frac{\mathcal{V}_i \Theta_{v,i} \mathrm{R}^0 / \mathcal{M}_i}{\exp(\Theta_{v,i} / T_{ve}) - 1}, \tag{15}$$

$$e_{e,i} = \frac{\mathrm{R}^0 T_{ve}^2}{\mathcal{M}_i} \frac{\partial}{\partial T_{ve}} \left(\ln Q_{e,i} \right). \tag{16}$$

In this formulation, $\Theta_{v,i}$ is the characteristic vibrational temperature of species i, while $Q_{e,i} = \sum_j g_{i,j} \exp(-\Theta_{e,i,j}/T_{ve})$ is the canonical partition function for the electronic energy mode of species i, with $\Theta_{e,i,j}$, and $g_{i,j}$ being, respectively, the characteristic temperature and degeneracy of the electronic energy level j. The first seven electronic energy levels are used for each species, with the characteristic temperature and degeneracy data taken from the NIST databases for atomic[1] and diatomic species.[2]

In this two-temperature approach, the sum of the vibrational and electronic-excitation specific internal energies

$$e_{ve} = \sum_{i=1}^{N_s} Y_i e_{ve,i} = \sum_{i=1}^{N_s} Y_i(e_{v,i} + e_{e,i}) \tag{17}$$

is described by the conservation equation [26]

$$\frac{\partial(\rho e_{ve})}{\partial t} + \nabla \cdot (\rho e_{ve} \mathbf{u}) = \nabla \cdot \left(\lambda_{ve} \nabla T_{ve} - \sum_{i=1}^{N_s} \rho Y_i \boldsymbol{V}_i e_{ve,i} \right) + \rho \sum_{i=1}^{N_s} Y_i \frac{e_{v,i}^* - e_{v,i}}{\tau_i} + \dot{w}_{ve}. \tag{18}$$

In Eq. (18), the second term on the right-hand side corresponds to exchange between the vibrational and translational energy modes [37], where $e_{v,i}^\star$ is the equilibrium vibrational internal energy calculated using expression (15) evaluated at the translational-rotational temperature T. Similarly, τ_i is a vibrational-relaxation time of species i given by [1]

$$\tau_i = \tau_i^P + \left(\sum_{j=1}^{N_s} \frac{X_j}{\tau_{ij}^{MW}} \right)^{-1}. \tag{19}$$

In this expression, τ_{ij}^{MW} is the vibrational-relaxation time, measured in seconds, proposed by Millikan and White [38], namely

$$\tau_{ij}^{MW} = \frac{1.01394 \times 10^{-3}}{P} \exp\left[\alpha_{ij} \left(T^{-1/3} - \beta_{ij} \right) \right], \tag{20}$$

which corresponds to molecule i colliding with species j, where P is in atm, T is in K, and the empirical constants α_{ij} and β_{ij} are taken from [25]. Additionally, τ_i^P represents the high-temperature correction given by [1]

$$\tau_i^P = \left[n\sigma_v \sqrt{(8\mathrm{R}^0 T / \pi \mathcal{M}_i)} \right]^{-1}, \tag{21}$$

where n is the number density, and σ_v is the following effective cross section measured in m^2 [25],

$$\sigma_v = 3 \times 10^{-21} \left(50{,}000/T \right)^2. \tag{22}$$

The dissociation/vibrational-excitation coupling term $\dot{w}_{ve}$ in Eq. (18) is modeled using the non-preferential dissociation model [39]

$$\dot{w}_{ve} = \sum_{i=1}^{N_s} \dot{w}_i e_{v,i}. \tag{23}$$

---

[1] Accessed 2021. https://physics.nist.gov/PhysRefData/ASD/levels_form.html.
[2] Accessed 2021. https://webbook.nist.gov/chemistry/.

3. Locally one-dimensional inviscid relations for hypersonic flows

In this Section, the derivation of LODI relations performed by Okong'o & Bellan [20] is extended to account for thermal non-equilibrium ($T \neq T_{ve}$). As in Refs. [17,19,20], the present derivation treats the flow through boundaries as locally one-dimensional and will not consider the effects of molecular transport, which are treated as higher-order corrections to these equations later in Section 4. Defining x as the boundary-normal coordinate and u as the corresponding velocity component, the one-dimensional inviscid equivalent of the conservation equations presented in Section 2 are expressed as

$$\frac{\partial \mathbf{U}}{\partial t} + \left[\left(\frac{\partial \mathbf{C}}{\partial \mathbf{U}} \right)^{-1} \frac{\partial \mathbf{F}}{\partial \mathbf{U}} \right] \frac{\partial \mathbf{U}}{\partial x} = \left(\frac{\partial \mathbf{C}}{\partial \mathbf{U}} \right)^{-1} \mathcal{W}, \tag{24}$$

where

$$\mathbf{U} = [\rho,\ Y_1,\ Y_2, ... Y_{N_s},\ u,\ v,\ w,\ P,\ T_{ve}]^T, \tag{25}$$

is taken to be the vector of primitive variables. The vectors of conserved variables $\mathbf{C}$, inviscid fluxes $\mathbf{F}$ and reactive source terms $\mathcal{W}$ are defined respectively as

$$\mathbf{C} = \left[\rho,\ \rho Y_1,\ ... \rho Y_{N_s},\ \rho u,\ \rho v,\ \rho w,\ \rho E,\ \rho e_{ve} \right]^T, \tag{26}$$

$$\mathbf{F} = \left[\rho u,\ \rho u Y_1,\ ... \rho u Y_{N_s},\ \rho u^2 + P,\ \rho u v,\ \rho u w,\ \rho u H,\ \rho u e_{ve} \right]^T, \tag{27}$$

$$\mathcal{W} = \left[0,\ \dot{w}_1,\ \dot{w}_2, ... \dot{w}_{N_s},\ 0,\ 0,\ 0,\ 0,\ \sum_{i=1}^{N_s} \rho Y_i \frac{e_{v,i}^* - e_{v,i}}{\tau_i} + \dot{w}_{ve} \right]^T, \tag{28}$$

where $H = E + P/\rho$ is the stagnation enthalpy. Note that the continuity equation, obtained by summing Eq (1) over all species and applying the constraints $\sum_{i=1}^{N_s} Y_i = 1$ and $\sum_{i=1}^{N_s} \dot{w}_i = 0$, is retained here to facilitate the derivation of the characteristic boundary conditions but is not directly solved in the test cases presented below.

Upon performing the eigendecomposition of the bracketed matrix in (24), $\mathbf{A} = \mathbf{Y_R} \mathbf{\Lambda} \mathbf{Y_R}^{-1}$, and pre-multiplying by the matrix of right eigenvectors, the system of equations

$$\frac{\partial \mathbf{r}}{\partial t} + \mathbf{\Lambda} \frac{\partial \mathbf{r}}{\partial x} = \tilde{\mathcal{W}} \tag{29}$$

is obtained, where $\mathbf{r} = \mathbf{Y_R}^{-1} \mathbf{U}$ is the vector of Riemann invariants and $\tilde{\mathcal{W}}$ is an auxiliary vector defined as $\tilde{\mathcal{W}} = \mathbf{Y_R}^{-1} (\partial \mathbf{C}/\partial \mathbf{U})^{-1} \mathcal{W}$. Equivalently, the locally one-dimensional inviscid (LODI) relations for the primitive variables can be expressed compactly as

$$\frac{\partial \mathbf{U}}{\partial t} + \mathbf{Y_R} \mathcal{L} = \mathbf{Y_R} \tilde{\mathcal{W}}, \tag{30}$$

where $\mathcal{L} = \mathbf{\Lambda} (\partial \mathbf{r}/\partial x) = [\mathcal{L}_1, ... \mathcal{L}_{N_s+6}]^T$ is the vector of wave-amplitude variations, whose components are given by

$$\mathcal{L}_1 = (u - a) \left(\frac{\partial P}{\partial x} - \rho a \frac{\partial u}{\partial x} \right), \tag{31}$$

$$\mathcal{L}_2 = u \left(\frac{\partial P}{\partial x} - a^2 \frac{\partial \rho}{\partial x} \right), \tag{32}$$

$$\mathcal{L}_3 = u \frac{\partial v}{\partial x}, \tag{33}$$

$$\mathcal{L}_4 = u \frac{\partial w}{\partial x}, \tag{34}$$

$$\mathcal{L}_5 = u \frac{\partial T_{ve}}{\partial x}, \tag{35}$$

$$\mathcal{L}_{i+5} = u \frac{\partial Y_i}{\partial x}, \qquad i = 1, ..., N_s, \tag{36}$$

$$\mathcal{L}_{N_s+6} = (u + a) \left(\frac{\partial P}{\partial x} + \rho a \frac{\partial u}{\partial x} \right). \tag{37}$$

In the above expressions, the symbol a represents the thermochemically-frozen speed of sound, namely

$$a = \sqrt{\left(\frac{\overline{c}_{p,tr}}{\overline{c}_{v,tr}} \right) \left(\frac{P}{\rho} \right)}, \tag{38}$$

where $\overline{c}_{p,tr}$ and $\overline{c}_{v,tr}$ are the average translational-rotational components of the specific heats of the mixture at constant pressure and constant volume, respectively. Using the rigid-rotor model and assuming full excitation of both translational and rotational degrees of freedom, the translational-rotational specific heat at constant volume can be expressed as

$$\overline{c}_{v,tr} = (3/2)R^0 T/\overline{\mathcal{M}} + \sum_{i=1}^{N_s} Y_i \mathcal{V}_i R^0 T/\mathcal{M}_i. \tag{39}$$

Similarly, $\overline{c}_{p,tr}$ is given by Mayer's relation as

$$\overline{c}_{p,tr} = \overline{c}_{v,tr} + R^0/\overline{\mathcal{M}}. \tag{40}$$

In comparing the wave-amplitude variations (31)-(37) obtained in this Section to those of Okong'o & Bellan [20], the wave-amplitude variation $\mathcal{L}_5$ given by Eq. (35) arises as new in the present study due to the consideration of thermal non-equilibrium. The associated Riemann invariant is the vibrational-electronic temperature, with a wave speed corresponding to the convective velocity normal to the boundary.

Expanding Eq. (30), the resulting set of equations can be expressed in terms of the wave-amplitude variations as

$$\frac{\partial \rho}{\partial t} + \frac{1}{a^2}\left(\frac{\mathcal{L}_1 + \mathcal{L}_{N_s+6}}{2} - \mathcal{L}_2\right) = 0, \tag{41}$$

$$\frac{\partial u}{\partial t} + \frac{1}{2\rho a}\left(\mathcal{L}_{N_s+6} - \mathcal{L}_1\right) = 0, \tag{42}$$

$$\frac{\partial v}{\partial t} + \mathcal{L}_3 = 0, \tag{43}$$

$$\frac{\partial w}{\partial t} + \mathcal{L}_4 = 0, \tag{44}$$

$$\frac{\partial P}{\partial t} + \frac{1}{2}\left(\mathcal{L}_{N_s+6} + \mathcal{L}_1\right) = \left(1 - \frac{\overline{c}_{p,tr}}{\overline{c}_{v,tr}}\right)\left[\rho \sum_{i=1}^{N_s} Y_i \frac{e_{v,i}^* - e_{v,i}}{\tau_i} + \dot{w}_{ve} + \sum_{i=1}^{N_s} \dot{w}_i\left(h_i - e_{ve,i} - \overline{c}_{p,tr}\frac{T\overline{\mathcal{M}}}{\mathcal{M}_i}\right)\right], \tag{45}$$

$$\frac{\partial T_{ve}}{\partial t} + \mathcal{L}_5 = \frac{1}{\overline{c}_{v,ve}}\left(\sum_{i=1}^{N_s} Y_i \frac{e_{v,i}^* - e_{v,i}}{\tau_i} - \sum_{i=1}^{N_s} \frac{\dot{w}_i e_{e,i}}{\rho}\right), \tag{46}$$

$$\frac{\partial Y_i}{\partial t} + \mathcal{L}_{i+5} = \frac{\dot{w}_i}{\rho}, \qquad i = 1, ..., N_s, \tag{47}$$

where $\overline{c}_{v,ve}$ is the constant-volume average specific heat corresponding to the vibrational-electronic energy modes of the mixture, which is given by

$$\overline{c}_{v,ve} = \sum_{i=1}^{N_s} Y_i\left(c_{v,v,i} + c_{v,e,i}\right), \tag{48}$$

where $c_{v,v,i}$ and $c_{v,e,i}$ are, respectively, the vibrational and electronic specific heats at constant volume for species i. The electronic specific heat for each species can be obtained from

$$c_{v,e,i} = \frac{R^0 T_{ve}}{\mathcal{M}_i}\left[2\frac{\partial}{\partial T_{ve}}\left(\ln Q_{e,i}\right) + T_{ve}\frac{\partial^2}{\partial T_{ve}^2}\left(\ln Q_{e,i}\right)\right]. \tag{49}$$

By making use of the harmonic-oscillator approximation, the vibrational specific heat can be expressed as

$$c_{v,v,i} = \frac{\mathcal{V}_i R^0}{\mathcal{M}_i}\left(\frac{\Theta_{v,i}}{T_{ve}}\right)^2 \frac{\exp(\Theta_{v,i}/T_{ve})}{\left[\exp(\Theta_{v,i}/T_{ve}) - 1\right]^2}. \tag{50}$$

Additionally, upon substituting the equation of state (9) into Eq. (45) and making use of Eqs. (41) and (47), the transport equation for the translational-rotational temperature

$$\frac{\partial T}{\partial t} + \frac{1}{2\rho\overline{c}_{p,tr}}\left(\mathcal{L}_{N_s+6} + \mathcal{L}_1\right) + \mathcal{L}_2/(\rho a^2/T) - T\overline{\mathcal{M}}\sum_{i=1}^{N_s}\mathcal{L}_{i+5}/\mathcal{M}_i = \frac{-1}{\overline{c}_{v,tr}}\left[\sum_{i=1}^{N_s} Y_i \frac{e_{v,i}^* - e_{v,i}}{\tau_i} + \frac{\dot{w}_{ve}}{\rho} + \sum_{i=1}^{N_s} \frac{\dot{w}_i}{\rho}\left(e_i - e_{ve,i}\right)\right] \tag{51}$$

is obtained. Equations (41)-(47) can be rewritten in conservation form as

$$\frac{\partial \rho}{\partial t} + d_1 = 0, \tag{52}$$

$$\frac{\partial \rho u}{\partial t} + \rho d_2 + u d_1 = 0, \tag{53}$$

$$\frac{\partial \rho v}{\partial t} + \rho d_3 + v d_1 = 0, \tag{54}$$

$$\frac{\partial \rho w}{\partial t} + \rho d_4 + w d_1 = 0, \tag{55}$$

$$\frac{\partial \rho E}{\partial t} + H d_1 + \rho \left(u d_2 + v d_3 + w d_4 \right) + \rho \bar{c}_{v,ve} d_5 + \rho \sum_{i=1}^{N_s} \left(h_i - \bar{c}_{p,tr} \frac{T \overline{\mathcal{M}}}{\mathcal{M}_i} \right) d_{i+5} + (\bar{c}_{p,tr} T) d_{N_s+6} = 0, \tag{56}$$

$$\frac{\partial \rho e_{ve}}{\partial t} + e_{ve} d_1 + \rho \bar{c}_{v,ve} d_5 + \rho \sum_{i=1}^{N_s} e_{ve,i} d_{i+5} = \rho \sum_{i=1}^{N_s} Y_i \frac{e_{v,i}^* - e_{v,i}}{\tau_i} + \dot{w}_{ve}, \tag{57}$$

$$\frac{\partial \rho Y_i}{\partial t} + \rho d_{i+5} + Y_i d_1 = \dot{w}_i, \qquad i = 1, ..., N_s, \tag{58}$$

where the symbols d_k are auxiliary variables defined as

$$d_1 = \frac{1}{a^2} \left(\frac{\mathcal{L}_1 + \mathcal{L}_{N_s+6}}{2} - \mathcal{L}_2 \right), \tag{59}$$

$$d_2 = \frac{1}{2\rho a} \left(\mathcal{L}_{N_s+6} - \mathcal{L}_1 \right), \tag{60}$$

$$d_3 = \mathcal{L}_3, \tag{61}$$

$$d_4 = \mathcal{L}_4, \tag{62}$$

$$d_5 = \mathcal{L}_5, \tag{63}$$

$$d_{i+5} = \mathcal{L}_{i+5}, \qquad i = 1, ..., N_s, \tag{64}$$

$$d_{N_s+6} = \mathcal{L}_2/a^2. \tag{65}$$

Equations (51)-(58), along with the supplementary variables (59)-(65), represent the LODI relations for high-enthalpy hypersonic flows in thermochemical non-equilibrium. The quantities d_k defined in Eqs. (59)-(65) are largely consistent with analogous expressions presented in Ref. [20]. In addition to the different speed of sound (38) arising in this study compared to that in Ref. [20], the element d_5 defined in Eq. (63) emerges here as new due to the presence of thermal non-equilibrium. Specifically, d_5 corresponds exactly to the convective term in the vibrational-electronic temperature equation (46). Furthermore, since the vibrational-electronic temperature is itself a Riemann invariant, d_5 is equal to the wave-amplitude variation $\mathcal{L}_5$.

4. Navier-Stokes characteristic boundary conditions for hypersonic flows

In this section, the LODI relations (52)-(58) are employed to provide a set of NSCBCs. In this discussion, as well as in the benchmark test cases presented in Section 5, the diffusion fluxes are incorporated in the description following similar approximations and methodologies to those described in Poinsot & Lele [17] and Okong'o & Bellan [20].

The description begins by assuming that the normal derivatives of the shear stresses tangential to the boundary are negligible,

$$\frac{\partial \tau_{xy}}{\partial x} = \frac{\partial \tau_{xz}}{\partial x} = 0, \tag{66}$$

where $\tau_{xy} = \hat{e}_1^T \overline{\overline{\tau}} \hat{e}_2$ and $\tau_{xz} = \hat{e}_1^T \overline{\overline{\tau}} \hat{e}_3$ can be defined in compact form as a function of the unit vectors $\hat{e}_1$, $\hat{e}_2$, and $\hat{e}_3$ in the x, y, and z directions, respectively. In addition, the normal derivative of the normal component of the mass diffusion flux is also taken to be negligible,

$$\frac{\partial \left(\rho Y_i V_{i,x} \right)}{\partial x} = 0, \qquad i = 1, ..., N_s. \tag{67}$$

Lastly, consistent with the prescription of zero normal derivative of the normal heat flux made by Poinsot & Lele [17], in this two-temperature description an analogous condition at the boundary can be expressed as

$$\frac{\partial}{\partial x} \left(\lambda_{rt} \frac{\partial T}{\partial x} \right) = \frac{\partial}{\partial x} \left(\lambda_{ve} \frac{\partial T_{ve}}{\partial x} \right) = 0. \tag{68}$$

Therefore, the relevant NSCBCs for high-enthalpy hypersonic flows can be expressed as

$$\frac{\partial \rho u}{\partial t} + \rho d_2 + u d_1 = \frac{\partial \tau_{xx}}{\partial x} - \nabla_t \cdot \left(\rho u \boldsymbol{u_t} \right), \tag{69}$$

$$\frac{\partial \rho v}{\partial t} + \rho d_3 + v d_1 = -\frac{\partial P}{\partial y} + \nabla_t \cdot \left(\boldsymbol{\tau_{yt}} \right) - \nabla_t \cdot \left(\rho v \boldsymbol{u_t} \right), \tag{70}$$

$$\frac{\partial \rho w}{\partial t} + \rho d_4 + w d_1 = -\frac{\partial P}{\partial z} + \nabla_t \cdot \left(\boldsymbol{\tau_{zt}} \right) - \nabla_t \cdot \left(\rho w \boldsymbol{u_t} \right), \tag{71}$$

$$\frac{\partial \rho E}{\partial t} + H d_1 + \rho \left(u d_2 + v d_3 + w d_4 \right) + \rho \bar{c}_{v,ve} d_5 + \rho \sum_{i=1}^{N_s} \left(h_i - \bar{c}_{p,tr} \frac{T \overline{\mathcal{M}}}{\mathcal{M}_i} \right) d_{i+5} + (\bar{c}_{p,tr} T) d_{N_s+6}$$
$$= \frac{\partial \left(u \tau_{xx} \right)}{\partial x} + \tau_{xy} \frac{\partial v}{\partial x} + \tau_{xz} \frac{\partial w}{\partial x} - \rho \sum_{i=1}^{N_s} Y_i V_{i,x} \frac{\partial h_i}{\partial x} + \nabla_t \cdot \left(\overline{\overline{\tau_t}} \boldsymbol{u_t} + \lambda_{tr} \nabla_t T + \lambda_{ve} \nabla_t T_{ve} - \rho \sum_{i=1}^{N_s} Y_i \boldsymbol{V_{i,t}} h_i - \rho H \boldsymbol{u_t} \right), \tag{72}$$

$$\frac{\partial \rho e_{ve}}{\partial t} + e_{ve}d_1 + \rho \bar{c}_{v,ve}d_5 + \rho \sum_{i=1}^{N_s} e_{ve,i}d_{i+5} = \rho \sum_{i=1}^{N_s} Y_i \frac{e_{v,i}^* - e_{v,i}}{\tau_i} + \dot{w}_{ve} - \rho \sum_{i=1}^{N_s} Y_i V_{i,x} \frac{\partial e_{ve,i}}{\partial x}$$
$$+ \nabla_t \cdot \left(\lambda_{ve} \nabla_t T_{ve} - \rho \sum_{i=1}^{N_s} Y_i \boldsymbol{V}_{i,t} e_{ve,i} - \rho e_{ve} \boldsymbol{u_t} \right), \tag{73}$$

$$\frac{\partial \rho Y_i}{\partial t} + \rho d_{i+5} + Y_i d_1 = \dot{w}_i - \nabla_t \cdot \left[\rho Y_i \left(\boldsymbol{V}_{i,t} + \boldsymbol{u_t} \right) \right], \qquad i = 1, ..., N_s, \tag{74}$$

where $\nabla_t = [\partial/\partial y,\ \partial/\partial z]^T$ is the transverse nabla operator, $\boldsymbol{u_t} = [v,\ w]^T$ is the transverse velocity vector, $\tau_{xx} = \hat{\boldsymbol{e}}_1^T \bar{\bar{\tau}} \hat{\boldsymbol{e}}_1$ is the normal viscous stress, and $\boldsymbol{V}_{i,t} = [\hat{\boldsymbol{e}}_2,\ \hat{\boldsymbol{e}}_3]^T \boldsymbol{V}_i$ is the transverse diffusion-velocity vector, and $\bar{\bar{\tau_t}}$ is the transverse viscous stress tensor defined as

$$\bar{\bar{\tau_t}} = \begin{bmatrix} \tau_{yt}^T \\ \tau_{zt}^T \end{bmatrix} = [\hat{e}_2,\ \hat{e}_3]^T \bar{\bar{\tau}} [\hat{e}_2,\ \hat{e}_3]. \tag{75}$$

The NSCBCs (69)-(74) are employed in simulating the test cases studied below in Section 5. They are only applicable to the definition of the diffusion velocity (2), which neglects the effects of thermal diffusion and barodiffusion. Inclusion of these effects would require not only a modification of Eq. (2), but also the incorporation of the reciprocal Dufour effect in Eqs. (11) and (18), which would lead to extended versions of Eqs. (72)-(73).

The right-hand sides of Eqs. (69)-(74) are comprised of both inviscid and diffusive fluxes, as well as source terms, and can be evaluated directly at the boundaries with a suitable discretization. In contrast, further evaluation of left-hand-side terms depends on both the local wave speeds and on the type of boundary condition imposed. To clarify those dependencies, summarized procedures for imposing these NSCBCs at inflow and outflows are provided below:

(a) For subsonic outflow boundary conditions, the wave-amplitude variations $\mathcal{L}_2$ through $\mathcal{L}_{N_s+5}$ are computed at the outflow boundaries using Eqs. (31)-(36) with an upwind-biased stencil. The wave-amplitude variation $\mathcal{L}_1$ is associated with an incoming wave for outflow boundaries with $u > 0$. Consequently, $\mathcal{L}_1$ must either be (a) set to zero to yield a completely non-reflecting boundary, or (b) set to weakly impose a far-field pressure with

$$\mathcal{L}_1 = \kappa \left(P - P_\infty \right), \tag{76}$$

where κ is an adjustable coefficient and P_∞ is a reference pressure [17]. Likewise, $\mathcal{L}_{N_s+6}$ is computed with Eq. (37). As proposed by Poinsot & Lele [17], the reflectivity coefficient for a strictly subsonic outflow is computed as

$$\kappa = \alpha a \left(1 - Ma_{max}^2 \right) / l, \tag{77}$$

where $\alpha = 0.25$ is a constant, Ma_{max} is the maximum Mach number along the outflow boundary, a is the local speed of sound given by Eq. (38), and l is a reference length scale. For outflow boundaries with $Ma_{max} = 1$, the reflectivity coefficient is instead computed as

$$\kappa = \alpha \left(a - u^2/a \right) / l. \tag{78}$$

The sensitivity of the numerical solutions to the choice of the reference length scale l proves to be relatively small, as discussed below in Section 5.2. For outflow boundaries with $u < 0$, $\mathcal{L}_1$ is computed with Eq. (31) whereas the outflow pressure is weakly imposed with $\mathcal{L}_{N_s+6} = \kappa \left(P - P_\infty \right)$. In both cases, d_1 through d_{N_s+6} are computed from the wave-amplitude variations using Eqs. (59)-(65), thereby enabling time-advancement of the conserved variables at the outflow boundaries using Eqs. (69)-(74).

(b) For supersonic outflow boundary conditions, all wave-amplitude variations are computed using Eqs. (31)-(37) with an upwind-biased stencil. As in the case of subsonic outflows, d_1 through d_{N_s+6} are calculated with Eqs. (59)-(65), and the conserved variables at the boundaries are subsequently advanced using Eqs. (69)-(74).

(c) For subsonic inflow boundary conditions, the viscous fluxes are neglected and the time-varying velocity components, translational-rotational temperature, vibrational-electronic temperature, and chemical composition are imposed explicitly. For inflow boundaries with $u > 0$, $\mathcal{L}_1$ corresponds to an outgoing wave and therefore is computed using Eq. (31) with a downwind scheme. $\mathcal{L}_{N_s+6}$ is evaluated with Eq. (37) for subsonic inflows with $u < 0$. Whichever wave-amplitude variation among $\mathcal{L}_1$ and $\mathcal{L}_{N_s+6}$ is not computed internally using downwind scheme is evaluated using Eq. (42) while making use of the discrete temporal derivative for the imposed x component of the velocity. Additionally, $\mathcal{L}_2$ is determined from Eq. (51), whereas d_1 is evaluated in terms of the aforementioned wave-amplitude variations using Eq. (59), with the density at the inflow being updated from Eq. (52). Lastly, the pressure at the inflow is determined via the equation of state (9).

(d) For supersonic inflow boundary conditions, the time-dependent velocity components, translational-rotational temperature, vibrational-electronic temperature, pressure, and chemical composition can be imposed explicitly with Dirichlet boundary conditions.

5. Canonical test cases

In order to evaluate the performance of the NSCBCs derived in the previous section, three benchmark cases are considered in which the boundary conditions are tested in high-enthalpy flows in thermochemical non-equilibrium representative of high-temperature post-shock conditions arising from incoming hypersonic freestream velocities. The first test case is a high-temperature vortex advected in supersonic flow in thermochemical non-equilibrium. The second test case consists of an interaction of a planar shock with a two-dimensional entropy wave in a high-temperature gas subject to thermochemical non-equilibrium effects. Lastly, the third test case is a three-dimensional shock/turbulence interaction problem subject to thermochemical non-equilibrium in the post-shock subsonic gas. The freestream operating conditions considered in all of these test cases correspond to continuum flows.

The NSCBCs are implemented in the Hypersonics Task-based Research (HTR) solver augmented with thermal non-equilibrium effects [40,41,13,42,43]. Whereas the diffusion fluxes are treated using a second-order central scheme, the Euler fluxes are discretized using a hybrid scheme that consists of a sixth-order skew-symmetric formulation hybridized with a sixth-order TENO scheme for shock-capturing [40,44,45]. In particular, the skew-symmetric scheme is deployed in the smooth regions of the flow and the TENO reconstruction is utilized for stencils that cross shock waves, which are detected using a modified Ducros sensor coupled with a TENO sensor based on the TENO-A stencil selection process. Further details on an assessment of the TENO flux reconstruction and hybridization procedure with application to high-speed two-temperature flows are provided in Refs. [42,43].

5.1. Non-equilibrium supersonic vortex advection

In this test case, a planar vortex is superposed with a uniform supersonic flow. This case resembles the vortex advection test considered in Okong'o & Bellan [20], but the configuration here is augmented with thermal non-equilibrium. In this case, the vortex does not simply advect, as there is also an evolution of the aerothermochemical field in the reference frame moving with the vortex because of acoustic expansion and finite rates of molecular transport and thermochemical relaxation, as shown in the results presented below.

The flow variables are normalized as follows. Both T and T_{ve} are normalized with the reference temperature $T_{ref} = 7000$ K, whereas P is normalized with the reference pressure $P_{ref} = 1.5$ kPa. The density is normalized with $\rho_{ref} = P_{ref}\mathcal{M}_{ref}/(R^0\ T_{ref})$ where $\mathcal{M}_{ref}$ is the molecular weight of the undissociated air. The velocity components are normalized with $u_{ref} = \sqrt{P_{ref}/\rho_{ref}}$. The reference length scale for the spatial coordinates is the vortex diameter $2R = 10$ cm. The time t is normalized with $t_{ref} = 2R/u_{ref}$.

Based on the reference values given above, the dimensionless streamwise velocity is prescribed initially as

$$u = U_\infty - 2y \exp\left[-2\left(x^2 + y^2\right)\right], \tag{79}$$

where $U_\infty = 5.0$ is the dimensionless free-stream velocity, which yields a free-stream Mach number of 4.2 and a Reynolds number $\rho_{ref}U_\infty u_{ref}L_{ref}/\mu_{ref} = 3500$, where μ_{ref} is the reference dynamic viscosity based on the initial temperature and composition. The initial dimensionless velocity in the y direction is given by

$$v = 2x \exp\left[-2\left(x^2 + y^2\right)\right]. \tag{80}$$

The initial dimensionless temperatures are uniform and equal $T = 1$ and $T_{ve} = 0.05$, whereas the initial dimensionless pressure is

$$P = 1 + \sqrt{\left(u - U_\infty\right)^2 + v^2}, \tag{81}$$

whose maximum value is $P = 1.6$. The initial composition corresponds to undissociated air, namely $X_{N_2} = 0.79$ and $X_{O_2} = 0.21$.

Two distinct computational domains, small and large, are considered in this study to verify that the numerical solution is insensitive to the position of the boundaries. The small computational domain extends a length of $18R$ and $12R$ in the x and y directions, respectively, such that $x \in [-6, 3]$ is discretized with 1440 grid points and $y \in [-3, 3]$ is discretized with 960 points. This resolution was chosen to provide a grid-converged numerical solution. Uniform spacing of grid points is utilized in each direction. The large computational domain is characterized by equal side lengths of $24R$, such that $\{x, y\} \in [-6, 6]$ with a total of 1920 points in each direction to maintain the same grid spacing as the small domain. NSCBCs are applied at the left and right boundaries of the computational domain, whereas periodicity is imposed at the top and bottom boundaries. Specifically, the left boundary serves as a supersonic inflow whereas the right behaves as a supersonic outflow.

The performance of the proposed NSCBCs under thermochemical non-equilibrium effects is shown in Figs. 1–6. Specifically, Figs. 1–3 demonstrate a correct preservation of the contours of pressure, density, and vibrational-electronic temperature as they cross the right boundary. In addition to the advection of the vortex itself, mean thermochemical relaxation proceeds from the inflow along the streamwise direction, which leads to the straight, transversal isocontours observed in the figures. Domain-size independence is proven by the consistency of all isocontours in the small and large domains.

Figs. 4–6 characterize the thermochemical state along the streamwise centerline of the computational domain. The results show the independence of the solution with respect to the streamwise length of the computational domain. As observed in Fig. 5, an appreciable slip between the two temperatures exists in this particular problem. Additionally, Fig. 6 indicates changes in chemical composition due to the evolution of the pressure and temperature fields in the vicinity of the vortex. The latter is able to advect successfully through the outflow boundary without any significant reflection of pressure disturbances from the outflow boundary, as shown in Figs. 1 and 4. Following the passage of the vortex, the vibrational-electronic temperature exhibits the expected monotonic
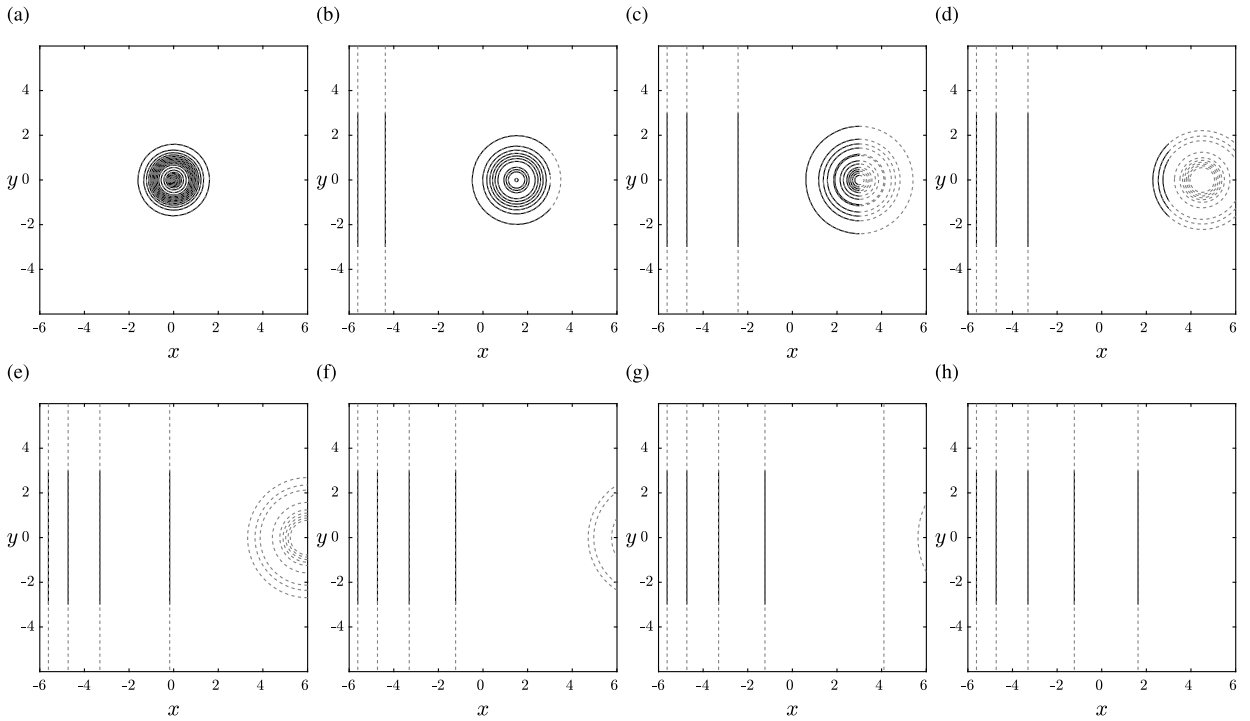
Fig. 1. Pressure contours at (a) $t = 0$, (b) 0.30, (c) 0.60, (d) 0.90, (e) 1.20, and (f) 1.50, (g) 1.80 and (h) 2.10 for non-equilibrium supersonic vortex advection. The twenty contour levels are equally spaced between $P = 0.65$ and $P = 1.65$. Solid and dashed lines correspond to small and large computational domains, respectively.

relaxation behavior towards the translational-rotational temperature, accelerating the dissociation reactions for the molecular species. This coupled thermochemical relaxation remains unaffected by the presence of the characteristic outflow boundary, as shown in Figs. 5 and 6.

In order to further characterize the performance of the characteristic boundary conditions, the error

$$\epsilon(\psi) = \sqrt{\frac{\int_\Omega (\psi - \tilde{\psi})^2 \, dx dy}{\int_\Omega \tilde{\psi}^2 \, dx dy}} \tag{82}$$

is defined, where ψ and $\tilde{\psi}$ represent any flow variable computed on the short and long domains, respectively. The integrals in both numerator and denominator of Eq. (82) are calculated in the short domain, which is denoted by Ω. Using a trapezoidal rule to approximate the error $\epsilon(\psi)$, the corresponding results are presented in Fig. 7 for five flow variables. In all cases, ϵ remains smaller than 10^{-5}, which demonstrates that the application of NSCBCs supports domain-independent solutions at supersonic convective velocities at thermochemical non-equilibrium conditions.

5.2. Non-equilibrium two-dimensional Shu-Osher shock tube

In this test case, a shock wave interacts with a two-dimensional entropy wave in a manner that resembles a two-dimensional analogue to the classic Shu-Osher problem [46], where additional consideration is given here to thermochemical non-equilibrium effects. The normalization approach employed for this test case is the same as that presented in Section 5.1, with $P_{Ref} = 500$ Pa, $T_{Ref} = 1000$ K, and $L_{Ref} = 1.0$ m. A shock wave located at $x = 0.5$ separates a high-pressure, high-temperature post-shock air on the left at Mach 1.3 in the laboratory reference frame, from its lower-pressure, lower-temperature pre-shock counterpart on the right. Isobaric variations in the initial density field are imposed in the pre-shock air that subsequently displace and corrugate the shock front.

The initial conditions for the problem in terms of dimensionless variables are

$$T_{ve} = T = \left\{ \begin{array}{ll} 5, & x < 0.5 \\ 1 + 0.25 \left[\cos(16\pi x) + \cos(16\pi y) \right], & x \geq 0.5 \end{array} \right\}, \tag{83}$$

$$P = \left\{ \begin{array}{ll} 15, & x < 0.5 \\ 1, & x \geq 0.5 \end{array} \right\}, \tag{84}$$

$$\mathbf{u} = \left\{ \begin{array}{ll} [4, 0]^T, & x < 0.5 \\ [0.30, 0]^T, & x \geq 0.5 \end{array} \right\}. \tag{85}$$
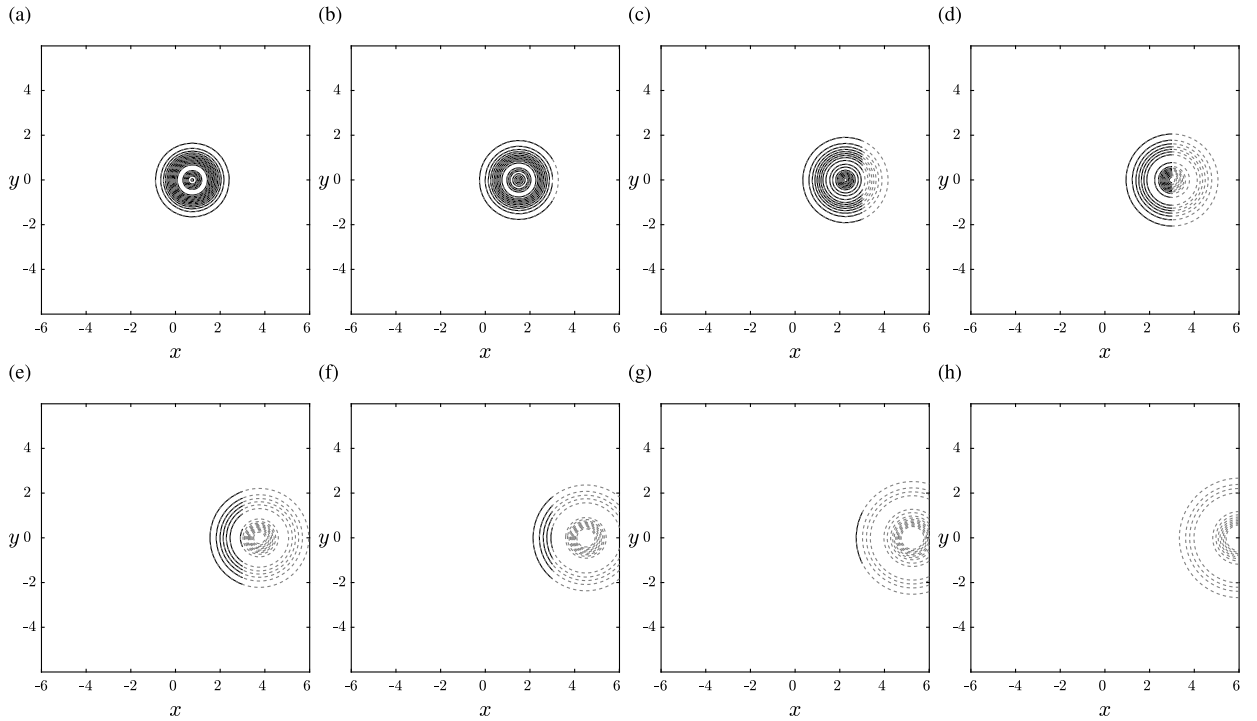
Fig. 2. Density contours at (a) $t = 0$, (b) 0.30, (c) 0.60, (d) 0.90, (e) 1.20, and (f) 1.50, (g) 1.80 and (h) 2.10 for non-equilibrium supersonic vortex advection. The twenty contour levels are equally spaced between $\rho = 0.85$ and $\rho = 1.65$. Solid and dashed lines correspond to small and large computational domains, respectively.

The composition field is initialized with chemical-equilibrium molar fractions in the post-shock air based on the local temperature and pressure. In contrast, in the pre-shock air, the composition field is initialized as thermochemically frozen, corresponding to $X_{N_2} = 0.79$ and $X_{O_2} = 0.21$.

Consistent with the analysis in Section 5.1, two distinct computational domains, short and long, are considered. The short domain is a square with side length of $L_x = L_y = 1$, such that $\{x, y\} \in [0, 1]$, and is discretized using 1280 uniformly-spaced grid points in each direction. This resolution was chosen to provide a grid-converged numerical solution. The long domain is a rectangle with $L_x = 2$ and $L_y = 1$, such that $y \in [0, 1]$ and $x \in [0, 2]$. The number of grid points is distributed uniformly and corresponds to 2560 and 1280 in the x and y directions, respectively, in such a way that the grid spacing in the x direction is the same for both domains. Characteristic boundary conditions are imposed in the streamwise direction, with the left boundary being a supersonic inflow and the right boundary being a subsonic outflow. The top and bottom boundary conditions enforce periodicity in the transversal direction.

The performance of the NSCBCs is demonstrated in Figs. 8–13. In particular, Fig. 8 provides the development of the density field throughout the interaction, which introduces not only vortical structures along the corrugated shock but also acoustic waves. The flow features are observed to exit the domain through the right boundary without causing any numerical artifact related to abnormal reflections. This satisfactory performance is achieved in the presence of the temperature slip introduced immediately behind the shock wave corresponding to the preferential excitation of translational-rotational energy, as observed by comparing the contours in Figs. 9 and 10, and more quantitatively by the one-dimensional profiles in Fig. 11. The thermal non-equilibrium is most apparent in Fig. 11(a) because of the continuity of the vibrational temperature across the shock. The post-shock gas is therefore characterized by thermal relaxation of the vibrational-electronic mode, along with chemical dissociation due to the high temperature. Furthermore, the comparisons made between the numerical solutions corresponding to the short and long computational domains in Fig. 11 for the temperature, Fig. 12 for the pressure, and Fig. 13 for the molar fractions, also indicate domain-size insensitivity despite the presence of subsonic convective velocities at the outflow and significant variations in thermodynamic quantities across the propagating discontinuity.

The error $\epsilon(\psi)$ defined in Eq. (82) is shown in Fig. 14 for simulations of this test case using two different values of the length scale $l = 0.1$ and $l = 1.0$ to calculate the outflow reflectivity coefficient (78). Comparison of the errors confirms that the performance of the proposed NSCBCs is largely insensitive to the choice of the length scale in computing the reflectivity coefficient, even in the presence of thermochemical non-equilibrium. In particular, the error remains small and of order 1% even when the outflow boundary is fully or partially subsonic, and therefore partially reflective due to the weak imposition of the far-field pressure. After the discontinuity exits the right boundary and the latter becomes a fully supersonic outflow, the error further decreases to levels comparable to those obtained in the test case for supersonic vortex advection.
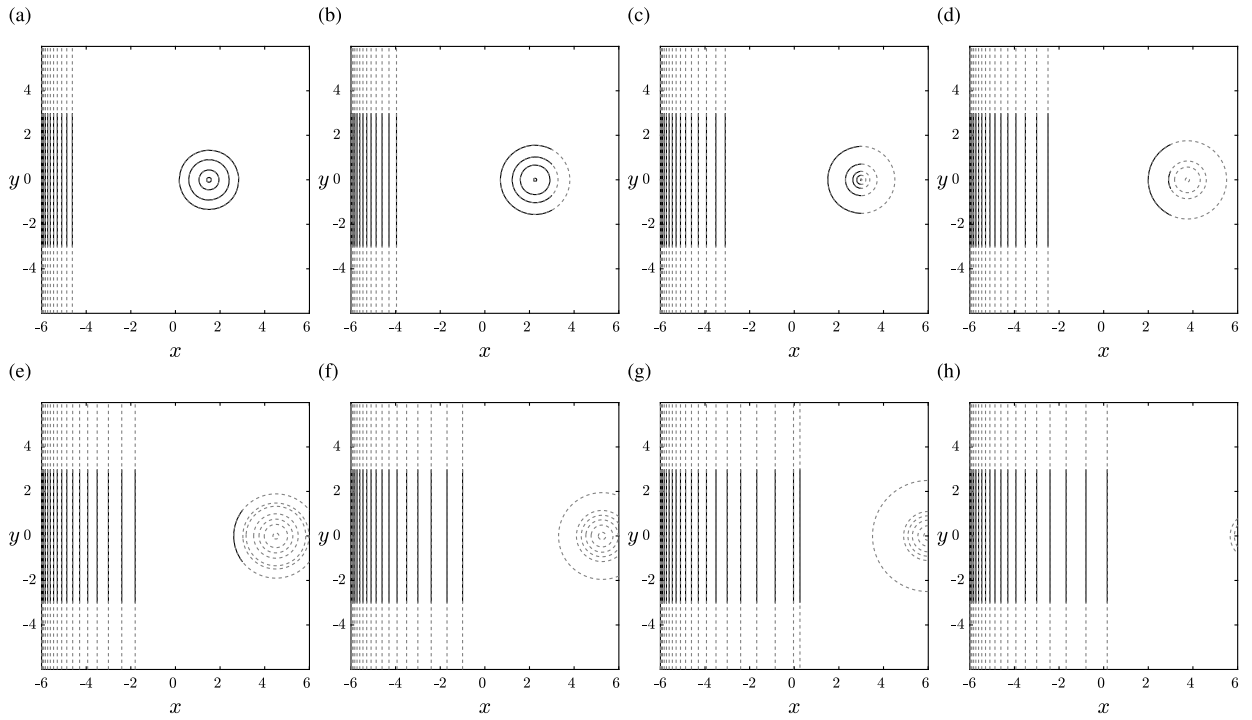
Fig. 3. Vibrational-electronic temperature contours at (a) $t = 0$, (b) 0.30, (c) 0.60, (d) 0.90, (e) 1.20, and (f) 1.50, (g) 1.80 and (h) 2.10 for non-equilibrium supersonic vortex advection. The twenty contour levels are equally spaced between $T_{ve} = 0.05$ and $T_{ve} = 0.65$. Solid and dashed lines correspond to small and large computational domains, respectively.
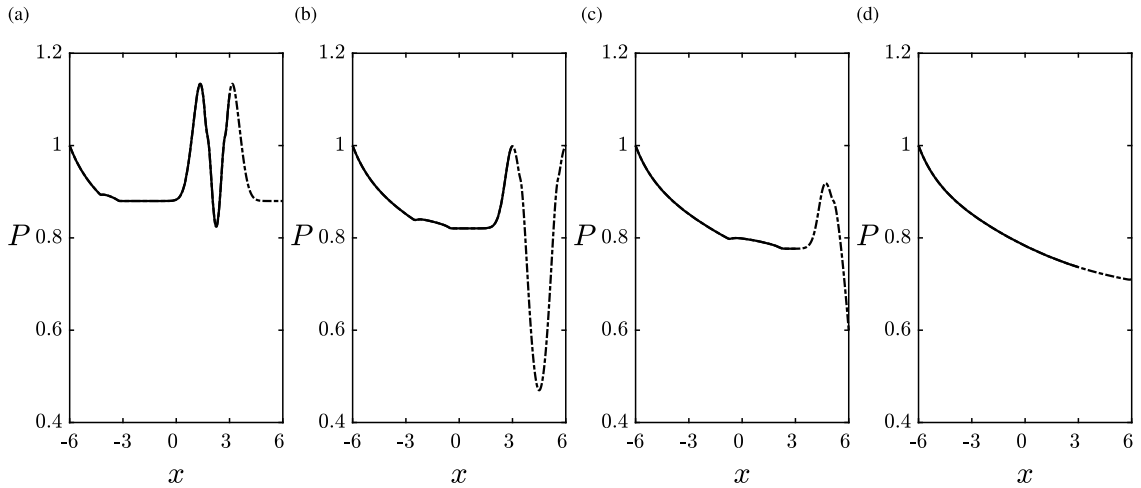

Fig. 4. Pressure profile along $y = 0$ at (a) $t = 0.45$, (b) 0.90, (c) 1.35, and (d) 3.00 for non-equilibrium supersonic vortex advection. Solid and dashed lines correspond to small and large computational domains, respectively, with $x = 0$ being the initial position of the vortex center.

5.3. Interaction of a shock wave with homogeneous isotropic turbulence including thermochemical non-equilibrium effects

In this closing test case, direct numerical simulations (DNS) of shock/turbulence interactions in thermochemical non-equilibrium are performed using the present computational framework, including the NSCBCs proposed in Section 4. Specifically, the non-reflective character of the proposed NSCBCs is evaluated in perhaps one of the most challenging cases that can be encountered, in which the outflow is subsonic, far from thermal equilibrium, and must support the treatment of acoustic waves induced by the shock/turbulence interaction. Since most previous simulations of this configuration have been performed at thermochemically frozen conditions (i.e., using the approximation of calorically perfect gases), it is worth providing here a short reference to early work. In particular, Lee et al. [7] performed a foundational simulation of shock/turbulence interactions quantifying the amplification of turbulent kinetic energy and transverse vorticity components across the shock in a calorically perfect gas. Subsequently, Refs. [47]
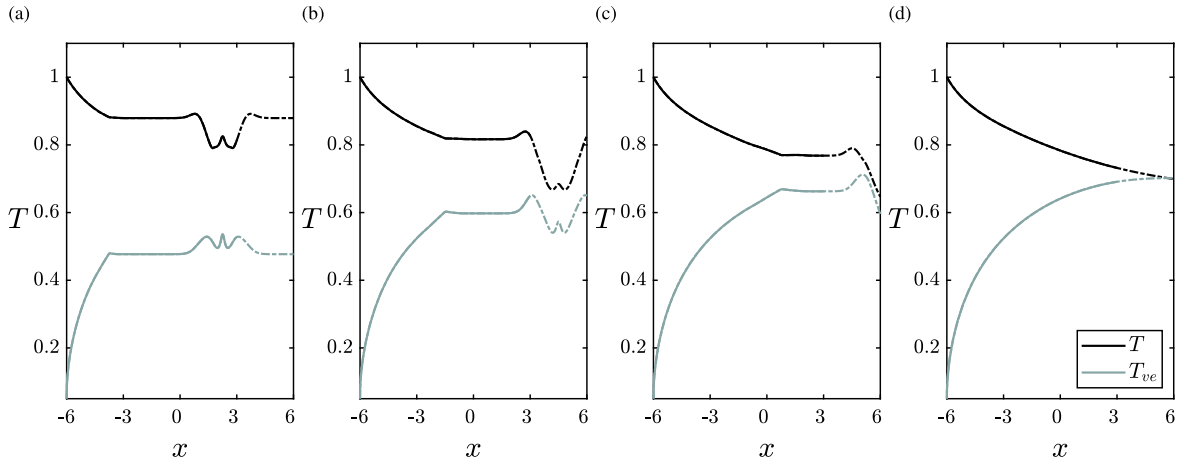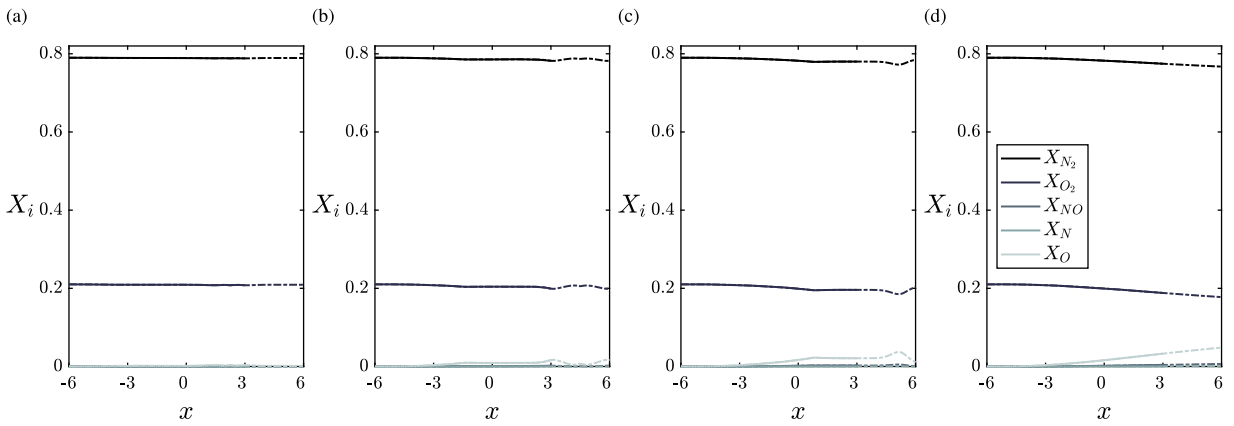
Fig. 5. Translational-rotational and vibrational-electronic temperature profiles along $y = 0$ at (a) $t = 0.45$, (b) 0.90, (c) 1.35, and (d) 3.00 for non-equilibrium supersonic vortex advection. Solid and dashed lines correspond to small and large computational domains, respectively, with $x = 0$ being the initial position of the vortex center.

Fig. 6. Molar fraction profiles along $y = 3$ at (a) $t = 0.45$, (b) 0.90, (c) 1.35, and (d) 3.00 for non-equilibrium supersonic vortex advection. Solid and dashed lines correspond to small and large computational domains, respectively, with $x = 0$ being the initial position of the vortex center.
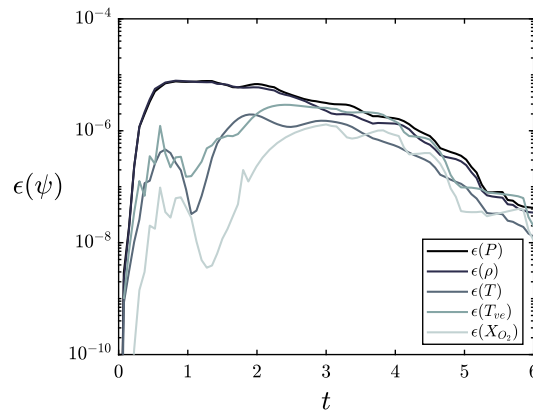
Fig. 7. Time history of the error (82) for non-equilibrium supersonic vortex advection.

and [48] characterized the impact of the Mach number and upstream entropy fluctuations on shock/turbulence interactions. An updated characterization of post-shock anisotropy in vorticity variances and Reynolds stresses was provided in Ref. [49], which also identified parameter ranges for which the incoming turbulence can annihilate the shock front. Equilibrium thermochemical effects were first introduced by Huete et al. [50] using linear interaction analysis (LIA). Enabled by the NSCBCs introduced in the present
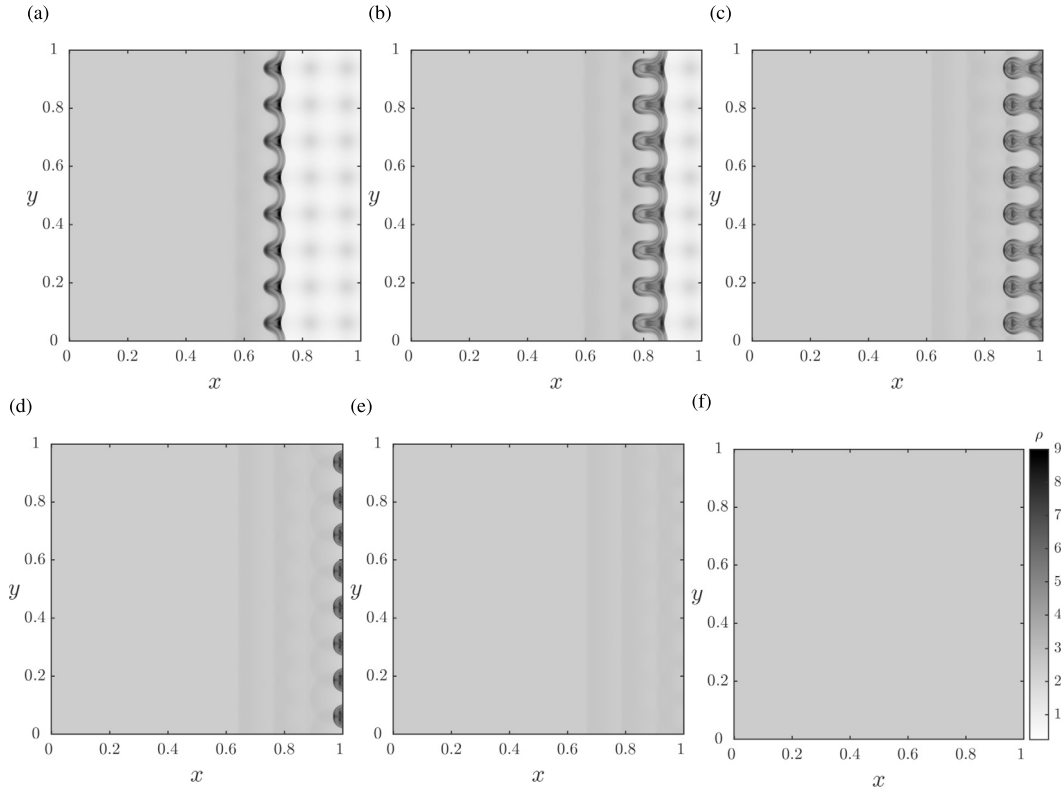
Fig. 8. Density contours at (a) $t = 0.05$, (b) 0.08, (c) 0.11, (d) 0.14, (e) 0.17, and (f) 1.00 for the two-dimensional Shu-Osher shock tube in the short computational domain.

manuscript, the DNS results reported here build on the linear analysis of Ref. [50] by characterizing shock/turbulence interactions with finite-rate chemistry, vibrational relaxation, and nonlinear dynamics. The analysis is not exhaustive, but nonetheless serves to exemplify the utilization of the proposed NSCBCs in a relevant case for engineering applications [51].

5.3.1. Computational setup

The overall computational setup for this final test case is comprised of two separate computational domains: the first domain, depicted in Fig. 15, contains the shock-turbulence interaction itself; the second domain (not shown here) is utilized for concurrently generating the homogeneous-isotropic-turbulence to be injected as inflow to the primary computational domain. The auxiliary homogeneous isotropic turbulence calculation is initialized with a divergence-free velocity field consistent with the exponential power spectrum of Passot & Poquet [52]

$$E(k) = 16\sqrt{\frac{2}{\pi}} \left(\frac{u_{rms}^2}{\kappa_0}\right) \left(\frac{\kappa^4}{\kappa_0^4}\right) \exp\left(\frac{-2\kappa^2}{\kappa_0^2}\right),$$ (86)

where κ is the dimensionless wavenumber, u_{rms} is the initial root mean square velocity, and $\kappa_0 = 2$ is the wavenumber with maximum energy density at initialization. For all cases presented below, the homogeneous isotropic turbulence is then linearly forced to preserve kinetic energy. The forcing follows the control-based method proposed in Ref. [53] by inserting a source term on the right-hand side of the momentum equation given by

$$\boldsymbol{\mathcal{F}}_{\rho u} = \rho \mathbb{A} (\boldsymbol{u} - \langle \boldsymbol{u} \rangle),$$ (87)

where $\langle \cdot \rangle$ denotes volume averaging and the coefficient $\mathbb{A}$ is computed to maintain constant kinetic energy as

$$\mathbb{A} = -\frac{\Pi + \Phi + (\mathcal{K} - \mathcal{K}_\infty)/\mathcal{T}}{2\mathcal{K}}.$$ (88)

In this formulation, Π is the volume-averaged pressure dilatation, Φ is the volume-averaged dissipation, $\mathcal{K} = (\langle \boldsymbol{u} \cdot \boldsymbol{u} \rangle - \langle \boldsymbol{u} \rangle \cdot \langle \boldsymbol{u} \rangle)/2$ is the turbulent kinetic energy, and $\mathcal{K}_\infty$ is the target-state kinetic energy, and $\mathcal{T} = 4\pi / (\kappa_0 u_{rms})$ is the chosen time-scale parameter for the physical-space forcing. The power input corresponding to the momentum forcing is then added to the right-hand side of the total energy equation as $\boldsymbol{\mathcal{F}}_{\rho E} = \boldsymbol{\mathcal{F}}_{\rho u} \cdot \boldsymbol{u} - \langle \boldsymbol{\mathcal{F}}_{\rho u} \cdot \boldsymbol{u} \rangle$ in order to preserve the total energy of the system. Sequential slices of the concurrent auxiliary simulation of homogeneous isotropic turbulence in a triply-periodic cubic domain are then imposed along with a uniform
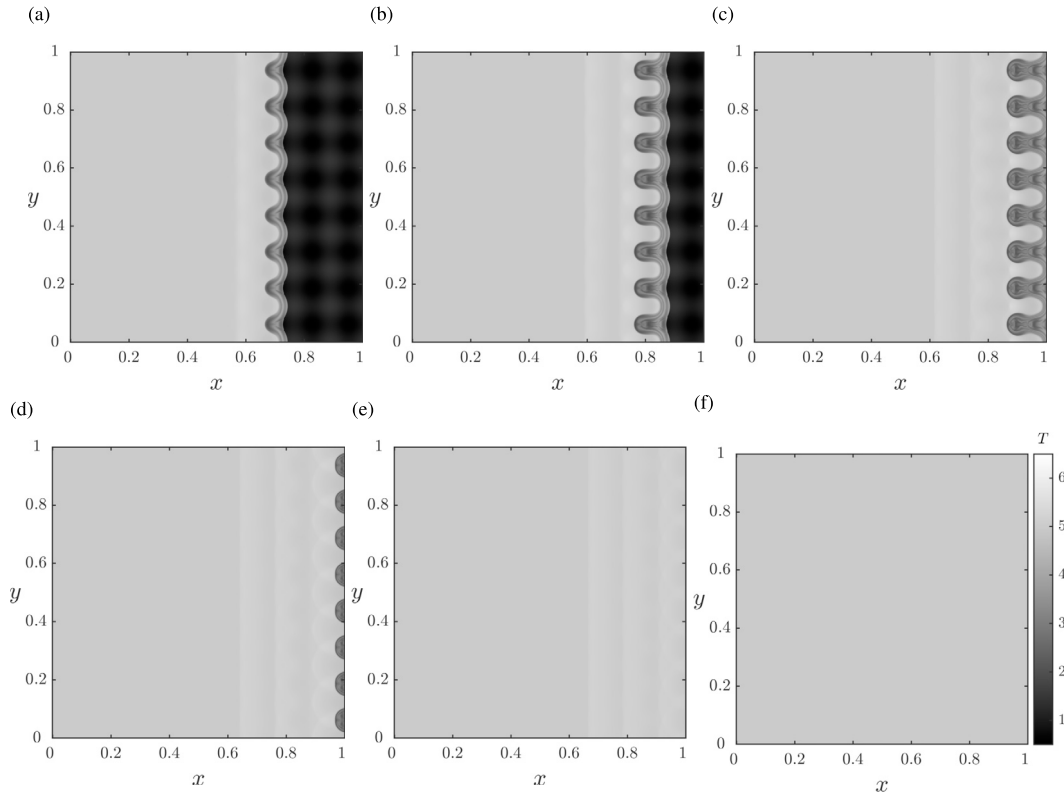
Fig. 9. Translational-rotational temperature contours at (a) $t = 0.05$, (b) 0.08, (c) 0.11, (d) 0.14, (e) 0.17, and (f) 1.00 for the two-dimensional Shu-Osher shock tube in the short computational domain.

supersonic stream in the $+x$ direction at the inflow $x = 0$ of the computational domain for the shock/turbulence interaction problem. The Taylor-Reynolds number and turbulent Mach number of the inflow turbulence are nominally 40 and 0.2, respectively. The mean values of the pressure and temperature in the inflow supersonic stream are 8.4 kPa and 700 K, respectively, thereby resulting in a pre-shock Mach number of 3 based on the mean values of the inflow velocity and speed of sound. The inflow chemical composition is that of thermochemically frozen air, namely $X_{N_2} = 0.79$ and $X_{O_2} = 0.21$. The inflow mean values of the flow variables are used for normalizing the results presented below.

The width of the computational domain is approximately 4π times the Taylor length, which is used for normalizing the spatial coordinates. Periodicity is imposed in the transverse directions y and z. An inviscid planar shock is initialized and let to freely evolve in time while becoming corrugated by the incident turbulence. The calculations are run for approximately 6 integral times before collecting statistics in order to flush away the transient. Statistics are collected over a period of 6 additional integral times while sampling the results at each time step. Favre-based planar averaging is performed across the transverse homogeneous directions.

As in the preceding test cases, the simulations are exercised in two computational domains of unequal streamwise length in order to analyze sensitivities to the placement of the outflow boundary. In particular, the short domain has a size $(L_x, L_y, L_z) = (12\pi, 4\pi, 4\pi)$ with a corresponding number of grid points of $1536 \times 240 \times 240$. This resolution was chosen to satisfy the DNS grid-resolution requirements described in Ref. [49]. The long domain enables further post-shock gas relaxation with an increased extent of $(L_x, L_y, L_z) = (24\pi, 4\pi, 4\pi)$ with $3072 \times 240 \times 240$ grid points, in such a way that the grid resolution is the same for both cases.

Furthermore, two types of outflow boundary conditions traditionally used in this configuration are also employed for comparisons. The first one (denoted as "NSCBC-only") is a NSCBC subsonic outflow in which the pressure is weakly imposed, as explained in Section 4. This approach suppresses drifting of the shock wave and facilitates collection of flow statistics. The second type (denoted as "sponge+NSCBC") is a classic, slab-shaped sponge whose width occupies the last 2π of the domain, corresponding to a total of 256 points in the x direction. A subsonic outflow NSCBC is applied on the leeward side of the sponge. Within the sponge region itself, a forcing vector $\mathcal{F}_s$ given by

$$\mathcal{F}_s = \frac{(x - x_B)^2}{4\pi^2}(C_T - C) \tag{89}$$

is added to the right-hand side of the conservation equations, consistent with the approach of Ref. [54]. In this formulation, x_B is the streamwise location of the windward side of the sponge, C is the vector of conserved variables defined in Eq. (26), and C_T is its corresponding target-state vector equivalent to the post-shock steady mean value. The latter must be informed by a coarser
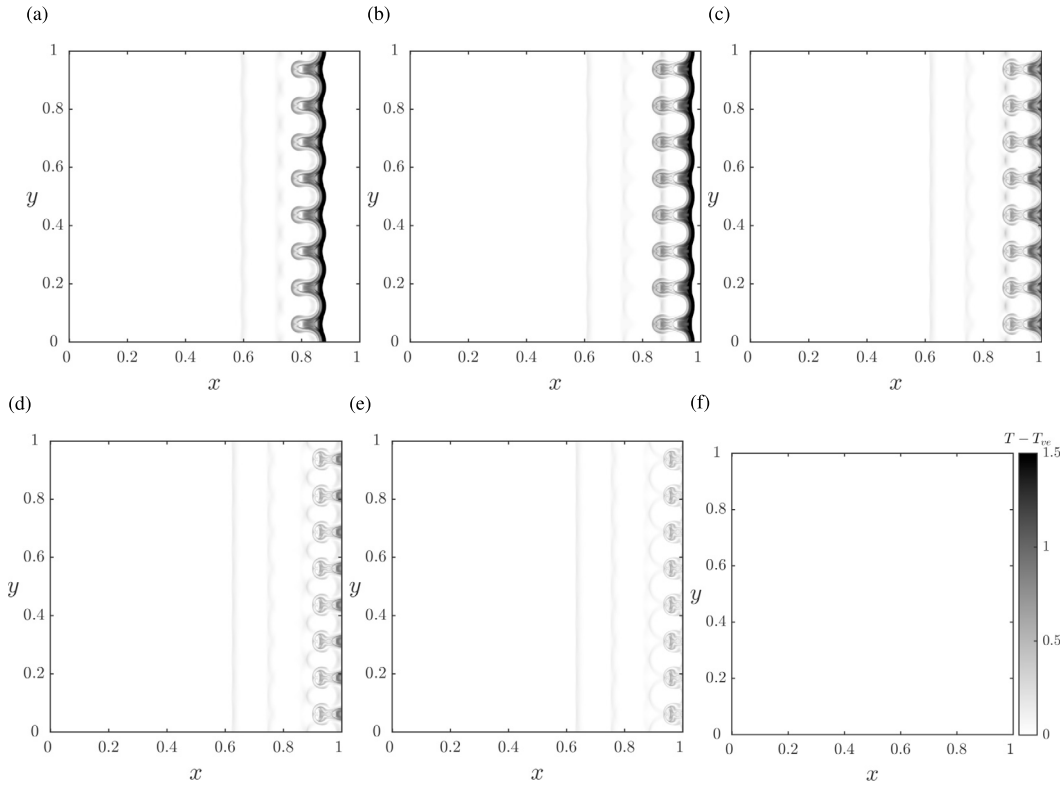
Fig. 10. Contours of thermal slip between the vibrational-electronic and translational-rotational temperatures at (a) $t = 0.08$, (b) 0.10, (c) 0.11, (d) 0.12, (e) 0.13, and (f) 1.00 for the two-dimensional Shu-Osher shock tube in the short computational domain.
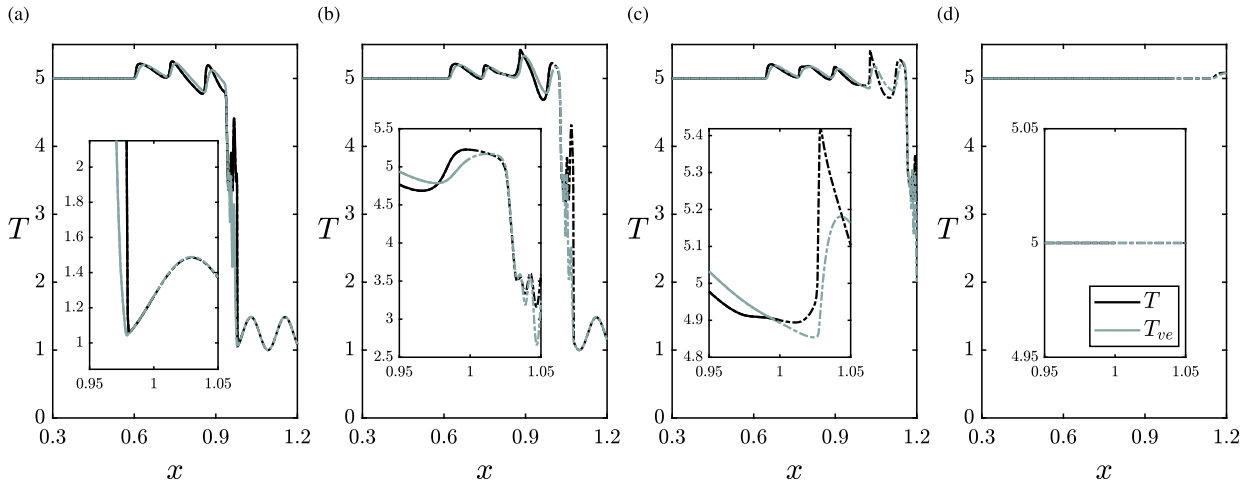

Fig. 11. Translational-rotational and vibrational-electronic temperature profiles along $y = 0.5$ at (a) $t = 0.10$, (b) 0.12, (c) 0.15, and (d) 0.70 for the two-dimensional Shu-Osher shock tube. Solid and dashed lines correspond to short and long computational domains, respectively.

simulation subjected to a NSCBC outflow boundary condition only (i.e., NSCBC-only), because the exit mean thermochemical state is unknown beforehand.

5.3.2. Results

Instantaneous cross-sectional contours of the thermal field computed with NSCBC-only conditions in the short domain are shown in Fig. 15. Specifically, Fig. 15(a,b) illustrates corrugations of the shock induced by the incident turbulent flow along with the amplification of fluctuations of both translational-rotational and vibrational-electronic temperatures across the shock. The resulting
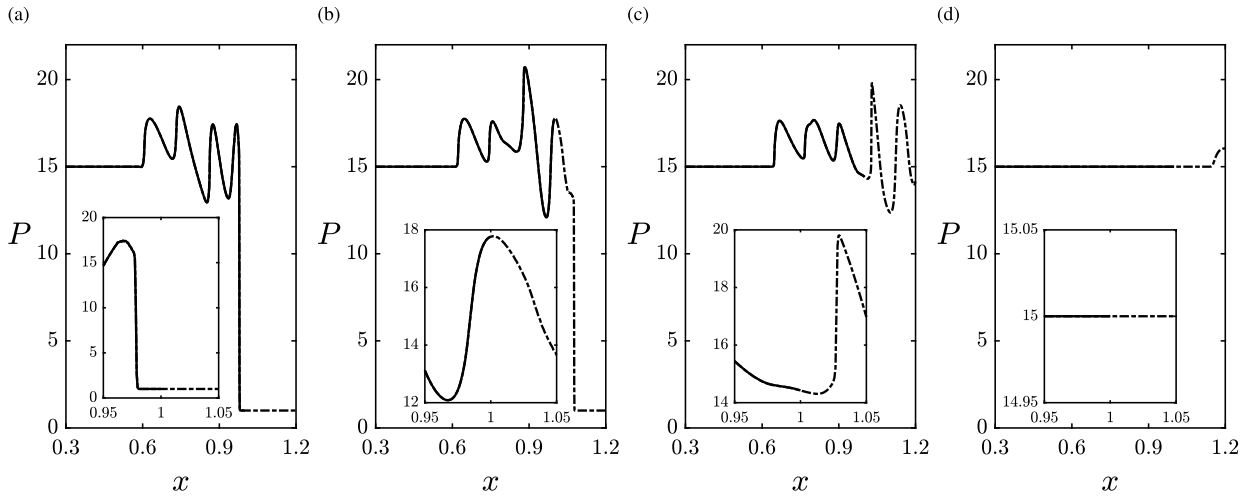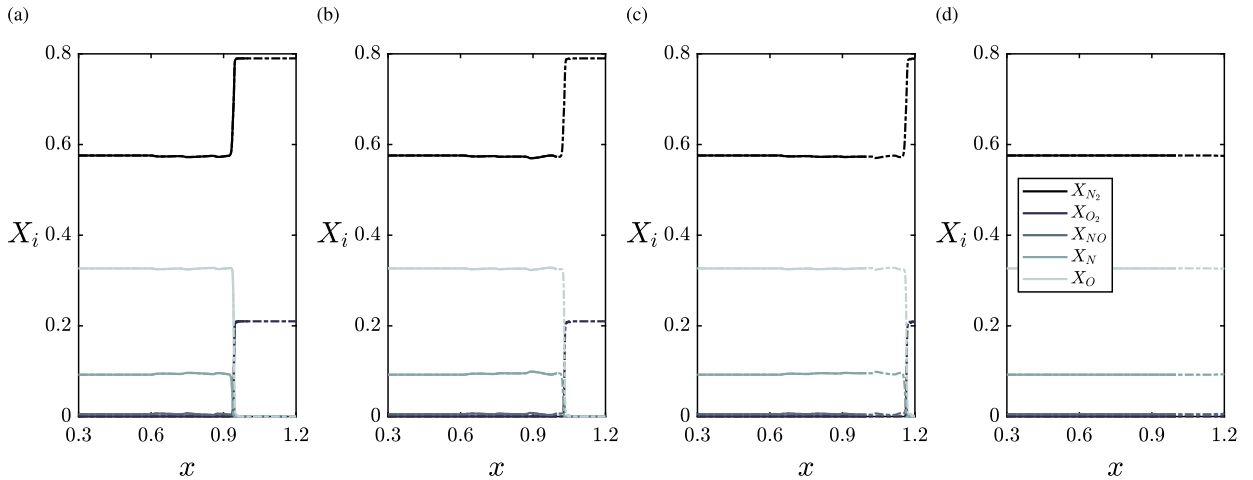
Fig. 12. Pressure profile along $y = 0.5$ at (a) $t = 0.10$, (b) 0.12, (c) 0.15, and (d) 0.70 for the two-dimensional Shu-Osher shock tube. Solid and dashed lines correspond to short and long computational domains, respectively.
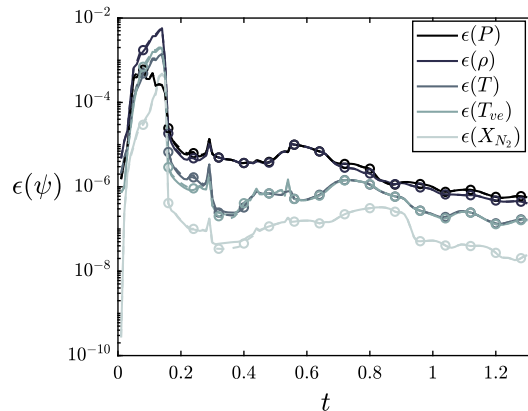
Fig. 13. Molar fraction profiles along $y = 0.5$ at (a) $t = 0.10$, (b) 0.12, (c) 0.15, and (d) 0.70 for the two-dimensional Shu-Osher shock tube. Solid and dashed lines correspond to short and long computational domains, respectively.

Fig. 14. Time history of the error (82) for the two-dimensional Shu-Osher shock tube. Solid lines designate the $l = 1.0$ case whereas the dashed lines with symbols denote the $l = 0.1$ case (largely indistinguishable from the solid lines).
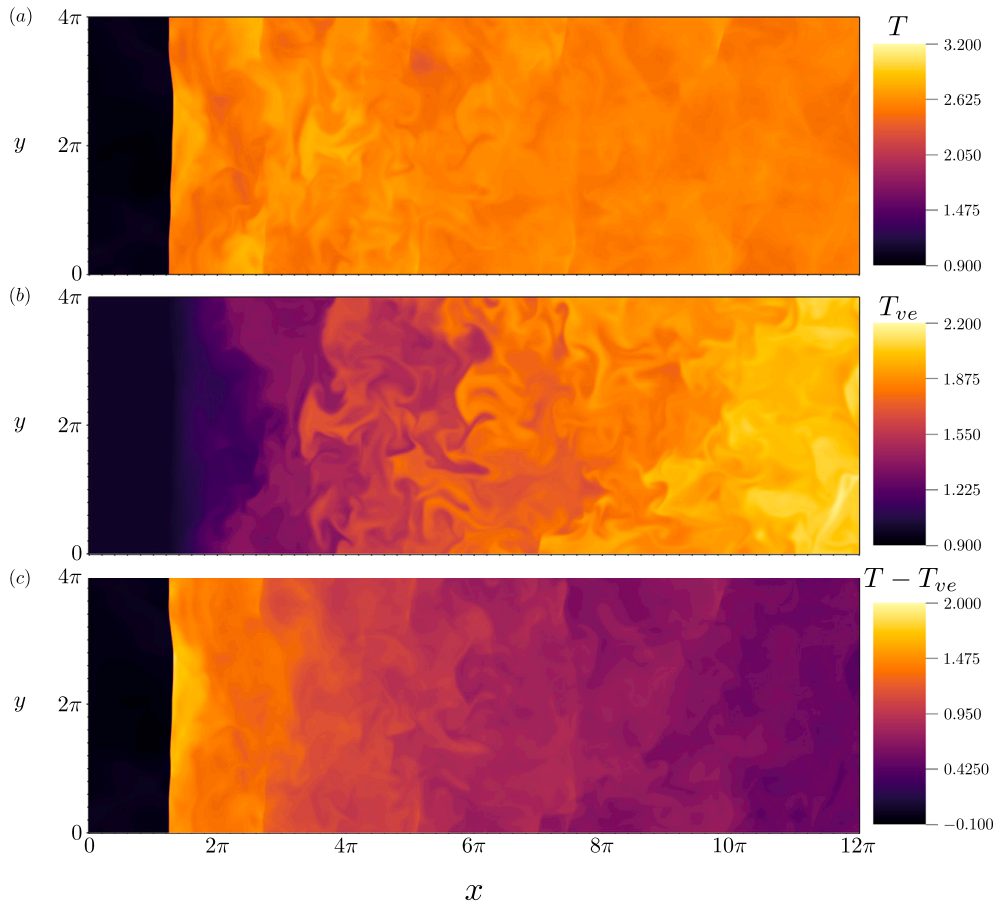
Fig. 15. Dimensionless instantaneous cross-sectional contours of (a) translational-rotational temperature, (b) vibrational-electronic temperature, and (c) temperature slip in shock-turbulence interaction with thermochemical non-equilibrium simulated with NSCBC-only conditions in the short computational domain.

maximum values of the temperature slip engendered by thermal non-equilibrium are found immediately downstream of the shock, as observed in Fig. 15(c). No numerical artifacts are detected in Fig. 15 near the outflow boundary.

Favre-based planar statistics are presented in Figs. 16–18 for the short and long domains in conjunction with NSCBC-only and sponge+NSCBC outflow conditions, with the origin of the x axis being shifted to the mean shock location $x = x_S$. As depicted in Fig. 16(a,b), significant vibrational-electronic non-equilibrium is induced by the presence of the normal shock, with vibrational relaxation proceeding through the outflow boundary of both short and long domains. This is accompanied by gradual variations in mean post-shock variables, including a streamwise deceleration in Fig. 17(a) along with slow increments in density and pressure in Fig. 18(a,b).

The location of the outflow boundary of the short domain is easily identifiable in the sponge+NSCBC case in Fig. 16(b,c), Fig. 17(b,c), and Fig. 18(c,d) because of the artificial suppression of all fluctuations near the boundary, as the target state C_T for the sponge is steady and uniform by definition. Equivalently, the volumetric forcing within the sponge region results in all variances tending to zero there. As a result, the solution computed with sponge+NSCBC outflow in the short domain departs significantly from its counterpart for the long domain near the interface between the two. It should however be stressed that the solution computed with sponge+NSCBC outflow performs satisfactorily throughout the rest of the domain and therefore remains a viable option.

In contrast, the solution computed with NSCBC-only conditions in the short domain follows much closely its counterpart in the long domain. Noticeable exceptions are the small overshoots in the variances of the translational-rotational temperature, streamwise velocity, density, and pressure observed near the outflow of the short domain in Figs. 16(c), 17(b), and 18(c,d). These discrepancies are engendered in the short domain by the partial reflectivity arising from weakly imposing the far-field pressure in order to maintain the shock stationary in the domain [47,49]. The impact of this partial reflectivity is most apparent in the density and pressure rms in the vicinity of the outflow boundary. The sponge+NSCBC simulation artificially suppresses these oscillations near the outflow by construction of the sponge. This artificial built-in suppression of fluctuations is absent in the NSCBC-only simulation. For these reasons, a domain-size independence study is always required for simulations using either one of the techniques (NSCBCs and sponges) or their combination.

In summary, these results suggest that the proposed NSCBC formulation performs adequately in preserving the main physical aspects of the problem and can be used by itself or in combination with a sponge, but the latter approach requires a coarser NSCBC-
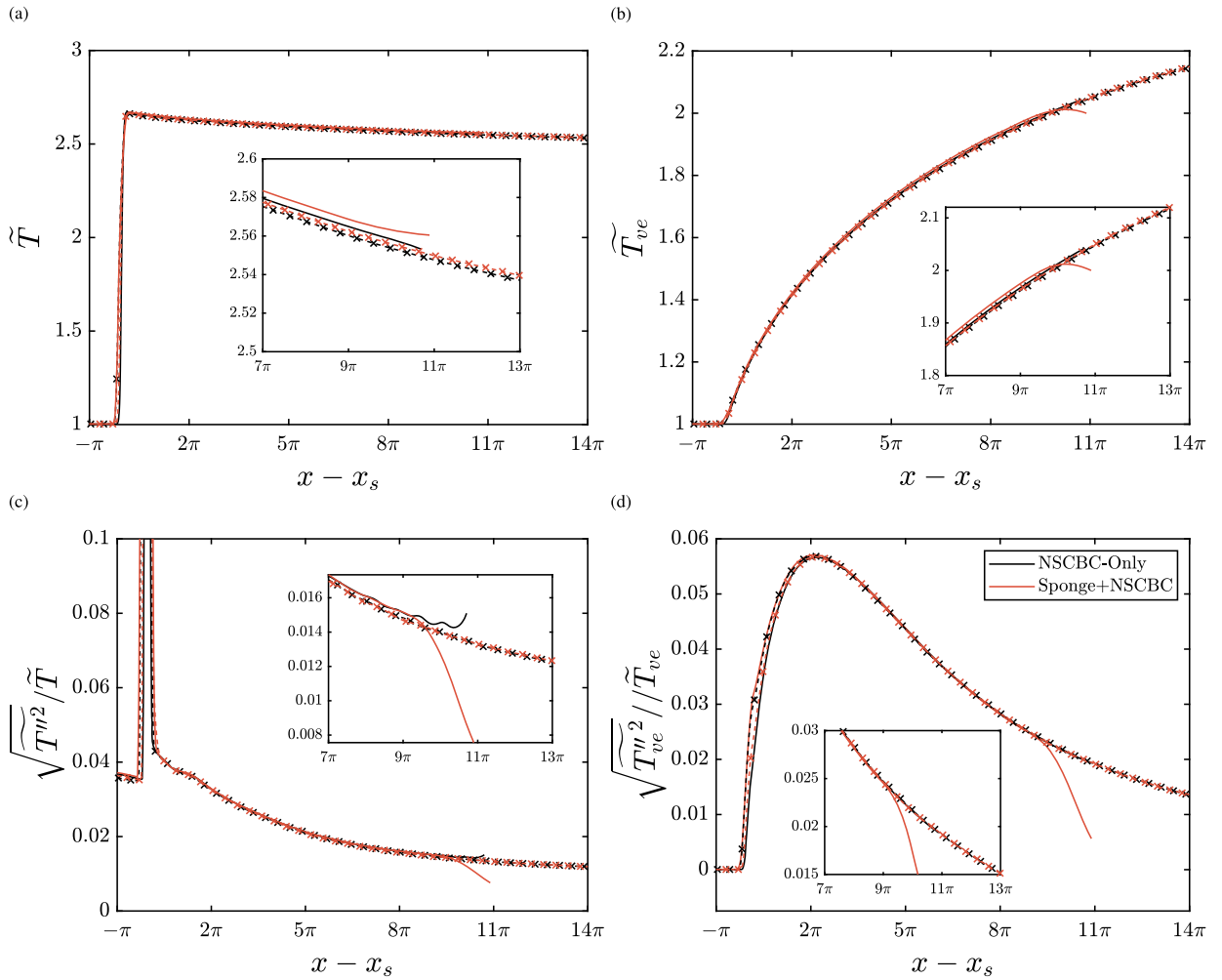
Fig. 16. Favre averages and root mean squares of (a,c) translational-rotational temperature and (b,d) vibrational-electronic temperature for shock-turbulence interaction with thermochemical non-equilibrium. Solid lines and lines with symbols indicate solutions computed in the short and long domains, respectively.

only simulation to provide an estimate for the sponge target state. Utilization of NSCBC-only conditions renders less sensitivity to the computational domain size and yields a maximum error between solutions computed in short and long domains of approximately 1% in the most relevant portion of the post-shock region.

6. Conclusions

In this study, NSCBCs for high-enthalpy hypersonic flows in thermochemical non-equilibrium have been proposed. The basis for the formulation consisted of relevant LODI relations derived for two-temperature conservation equations incorporating vibrational and chemical relaxation. The proposed NSCBCs were applied to three canonical test cases in thermochemical non-equilibrium, including a supersonic vortex advection, a two-dimensional Shu-Osher shock tube, and a shock/turbulence interaction problem. In all test cases, the proposed NSCBCs performed effectively in treating acoustic waves and flow structures crossing the boundaries without artificial reflections, while yielding solutions that were largely insensitive to the size of the computational domain. In the shock/turbulence interaction test case, utilization of the proposed NSCBCs without sponges enabled accurate enforcement of the outflow static pressure, thereby maintaining the planar shock stationary in the domain without introducing any significant numerical artifacts in the turbulence statistics near the shock. Naturally, the weak imposition of the outflow pressure necessarily renders the outflow boundary as partially reflective, although the ensuing numerical oscillations in density and pressure rms are largely confined to the immediate vicinity of the boundary in short domains, yielding a maximum error of approximately 1% in the most relevant portion of the shock/turbulence interaction. Using the proposed NSCBCs in conjunction with a sponge also rendered satisfactory results, rectifying in part the numerical oscillations present near the outflow boundary, though the resulting cost of the simulations using a sponge was higher since a suitable prediction of the sponge target thermochemical state required first an NSCBC-only simulation. The locally one-dimensional formulation of NSCBCs provided here is sufficient for simulating these canonical test
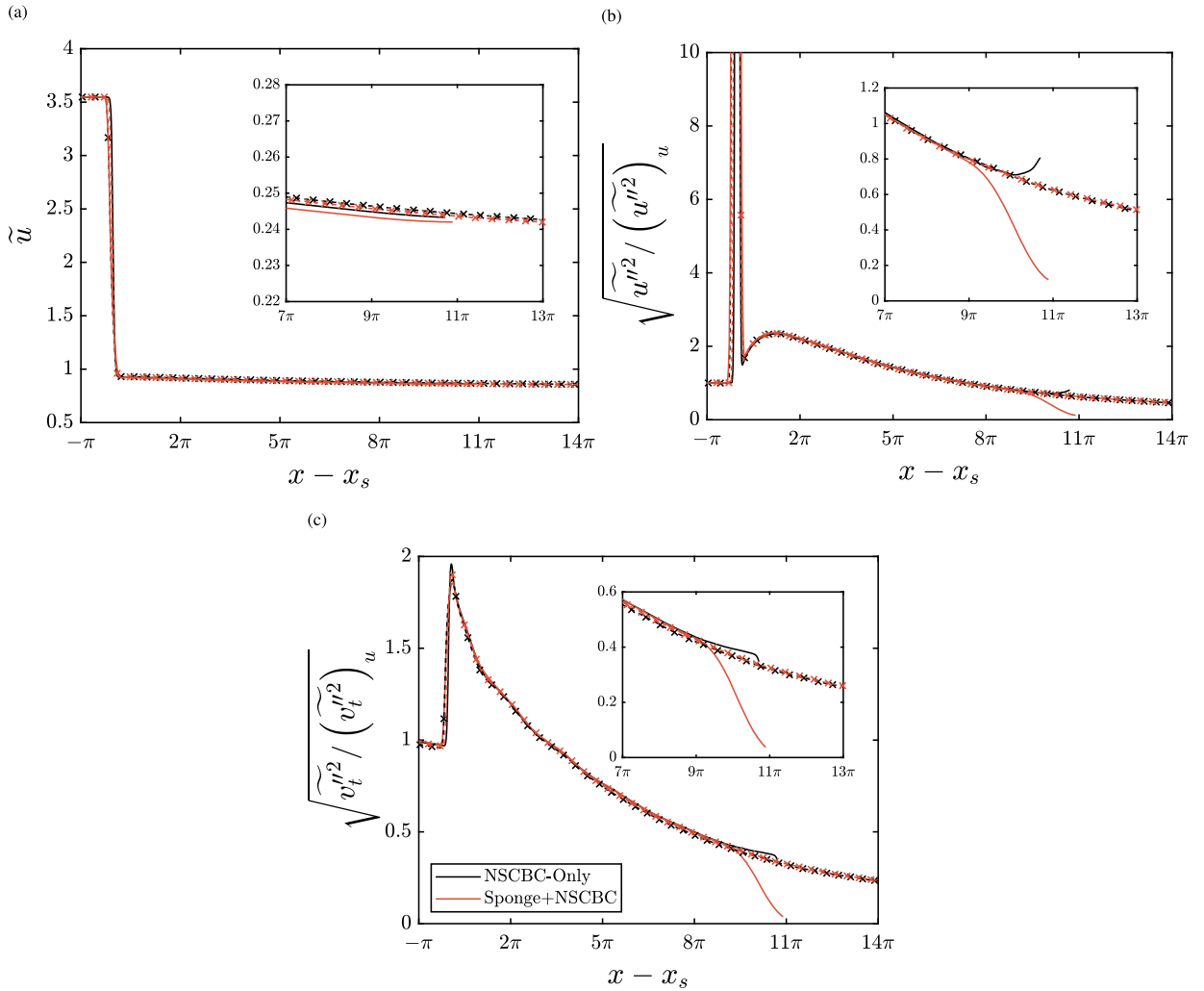
(a)

(b)

(c)

Fig. 17. (a) Favre-mean streamwise velocity along with Favre root mean squares (rms) of (b) streamwise and (c) spanwise velocity for shock-turbulence interaction with thermochemical non-equilibrium. Solid lines and lines with symbols indicate solutions computed in the short and long domains, respectively. The subindex u refers to the square of the fluctuation rms evaluated at the inflow plane.

cases. However, future worthwhile extensions of this work for more complex hypersonic flows in thermochemical non-equilibrium may involve incorporating three-dimensional effects in the formulation of the NSCBCs.

CRediT authorship contribution statement

Christopher Williams: Writing – review & editing, Writing – original draft, Software, Investigation, Formal analysis, Conceptualization. **Mario Di Renzo:** Writing – review & editing, Supervision, Software, Conceptualization. **Javier Urzay:** Writing – review & editing, Supervision, Conceptualization. **Parviz Moin:** Writing – review & editing, Supervision, Project administration, Conceptualization.

Declaration of competing interest

The authors declare that they have no known competing financial interests or personal relationships that could have appeared to influence the work reported in this paper.

Data availability
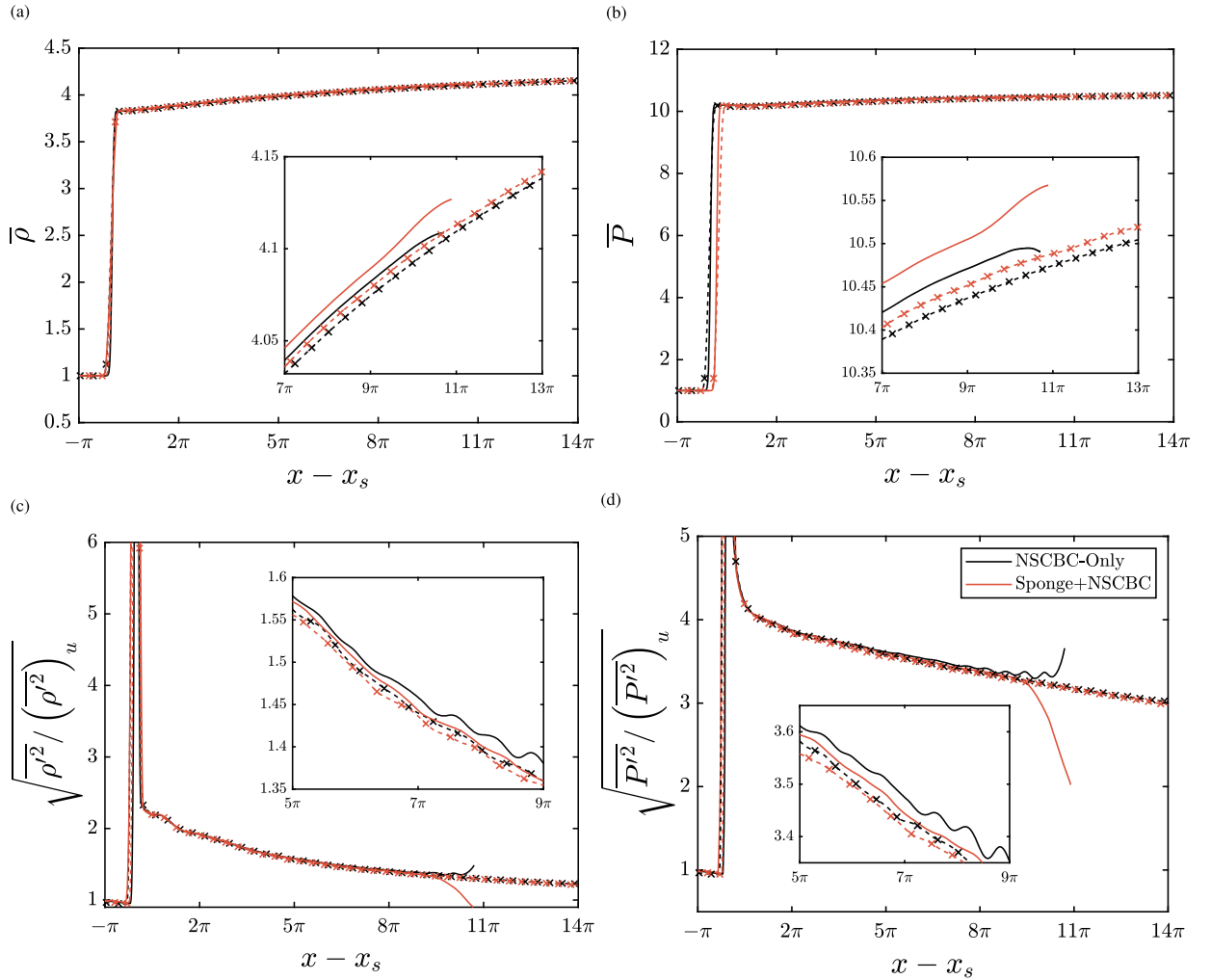
Data will be made available on request.

Fig. 18. Favre averages and root mean squares (rms) of (a,c) density and (b,d) pressure for shock-turbulence interaction with thermochemical non-equilibrium. Solid lines and lines with symbols indicate solutions computed in the short and long domains, respectively. The subindex u refers to the square of the fluctuation rms evaluated at the inflow plane.

Acknowledgements

References

[1] C. Park, Nonequilibrium Hypersonic Aerothermodynamics, Wiley, New York, 1990.

[2] S.P. Sharma, W.M. Huo, C. Park, Rate parameters for coupled vibration-dissociation in a generalized ssh approximation, J. Thermophys. Heat Transf. 6 (1992) 9–21.

[3] P.V. Marrone, C.E. Treanor, Chemical relaxation with preferential dissociation from excited vibrational levels, Phys. Fluids 6 (1963) 1215–1221.

[4] C.E. Treanor, P.V. Marrone, Effect of dissociation on the rate of vibrational relaxation, Phys. Fluids 5 (1962) 1022–1026.

[5] R.S. Chaudhry, I.D. Boyd, G.V. Candler, Vehicle-Scale Simulations of Hypersonic Flows Using the MMT Chemical Kinetics Model, AIAA Aviation Forum, 2020.

[6] G.V. Candler, Rate effects in hypersonic flows, Annu. Rev. Fluid Mech. 51 (2019) 379–402.

[7] S. Lee, S.K. Lele, P. Moin, Direct numerical simulation of isotropic turbulence interacting with a weak shock wave, J. Fluid Mech. 251 (1993) 533–562.

[8] S. Pirozzoli, F. Grasso, Direct numerical simulation of impinging shock wave/turbulent boundary layer interaction at m = 2.25, Phys. Fluids 18 (2006) 065113.

[9] M. Wu, M. Pino-Martin, Analysis of shock motion in shockwave and turbulent boundary layer interaction using direct numerical simulation data, J. Fluid Mech. 594 (2008) 71–83.

[10] J. Larsson, I. Bermejo-Moreno, S.K. Lele, Reynolds- and Mach-number effects in canonical shock–turbulence interaction, J. Fluid Mech. 717 (2013) 293–321.

[11] L. Fu, M. Karp, S.T. Bose, P. Moin, J. Urzay, Shock-induced heating and transition to turbulence in a hypersonic boundary layer, J. Fluid Mech. 909 (2021) A8.

[12] L. Duan, M.P. Martin, Direct numerical simulation of hypersonic turbulent boundary layers. Part 4. Effect of high enthalpy, J. Fluid Mech. 684 (2011) 25–59.

[13] M. Di Renzo, J. Urzay, Direct numerical simulation of a hypersonic transitional boundary layer at suborbital enthalpies, J. Fluid Mech. 912 (2021) A29.

[14] D. Passiatore, L. Sciacovelli, P. Cinnella, G. Pascazio, Thermochemical non-equilibrium effects in turbulent hypersonic boundary layers, J. Fluid Mech. 941 (2022) A21.

[15] K.W. Thompson, Time dependent boundary conditions for hyperbolic systems, J. Comput. Phys. 68 (1987) 1–24.

[16] K.W. Thompson, Time-dependent boundary conditions for hyperbolic systems, ii, J. Comput. Phys. 89 (1990) 439–461.

[17] T.J. Poinsot, S.K. Lele, Boundary conditions for direct simulations of compressible viscous flows, J. Comput. Phys. 101 (1992) 104–129.

[18] G. Lodato, P. Domingo, L. Vervisch, Three-dimensional boundary conditions for direct and large-eddy simulation of compressible viscous flows, J. Comput. Phys. 227 (2008) 5105–5143.

[19] M. Baum, T. Poinsot, D. Thévenin, Accurate boundary conditions for multicomponent reactive flows, J. Comput. Phys. 116 (1995) 247–261.

[20] N. Okong'o, J. Bellan, Consistent boundary conditions for multicomponent real gas mixtures based on characteristic waves, J. Comput. Phys. 176 (2002) 330–344.

[21] Y. Ju, J. Yuan, H. Kobayashi, G. Masuya, On the non-reflective boundary conditions for chemically reactive flows, AIAA Paper #2003-3969, 2003.

[22] A.T.C.S. Yoo, Y. Wang, H.G. Im, Characteristic boundary conditions for direct simulations of turbulent counterflow flames, Combust. Theory Model. 9 (2005) 617–646.

[23] A. Coussement, O. Gicquel, J. Caudal, B. Fiorina, G. Degrez, Three-dimensional boundary conditions for numerical simulations of reactive compressible flows with complex thermochemistry, J. Comput. Phys. 231 (2012) 5571–5611.

[24] P. Hammerling, J.D. Teare, B. Kivel, Theory of radiation from luminous shock waves in nitrogen, Phys. Fluids 2 (1959) 422–426.

[25] C. Park, Review of chemical-kinetic problems of future nasa missions. I - Earth entries, J. Thermophys. Heat Transf. 7 (1993) 385–398.

[26] P. Gnoffo, R. Gupta, J. Shinn, L. R. Center, U. S. N. Aeronautics, S. A. O. of Management, Conservation Equations and Physical Models for Hypersonic Air Flows in Thermal and Chemical Nonequilibrium, NASA technical paper, National Aeronautics and Space Administration, Office of Management, Scientific and Technical Information Division, 1989.

[27] C.F. Curtiss, J.O. Hirschfelder, Transport properties of multicomponent gas mixtures, J. Chem. Phys. 17 (1949) 550–555.

[28] T.P. Coffee, J.M. Heimerl, Transport algorithms for premixed, laminar steady-state flames, Combust. Flame 43 (1981) 273–289.

[29] A. Ern, V. Giovangigli, Multicomponent Transport Algorithms, Lecture Notes in Physics Monographs, Springer, Berlin, Heidelberg, 1994.

[30] C. Park, A review of reaction rates in high temperature air, AIAA Paper #AIAA-89-1740, 1989.

[31] C. Park, R.L. Jaffe, H. Partridge, Chemical-kinetic parameters of hyperbolic Earth entry, J. Thermophys. Heat Transf. 15 (2001) 76–90.

[32] L.C. Scalabrin, Numerical simulation of weakly ionized hypersonic flow over reentry capsules, Ph.D. thesis, University of Michigan, 2007.

[33] W.T. Maier, J.T. Needels, C. Garbacz, F. Morgado, J.J. Alonso, M. Fossati, Su2-nemo: an open-source framework for high-Mach nonequilibrium multi-species flows, Aerospace 8 (2021) 193.

[34] S.F. Gimelshein, I.J. Wysong, A.J. Fangman, D.A. Andrienko, O.V. Kunova, E.V. Kustova, F. Morgado, C. Garbacz, M. Fossati, K.M. Hanquist, Kinetic and continuum modeling of high-temperature air relaxation, J. Thermophys. Heat Transf. 36 (2022) 870–893.

[35] C.R. Wilke, A viscosity equation for gas mixtures, J. Chem. Phys. 18 (1950) 517–519.

[36] W.G. Vincenti, C.H. Krüger, Introduction to Physical Gas Dynamics, Wiley, New York, 1965.

[37] L. Landau, E. Teller, Zur Theorie der Schalldispersion, Phys. Z. Sowjetunion 10 (1) (1936) 34–43.

[38] R.C. Millikan, D.R. White, Systematics of vibrational relaxation, J. Chem. Phys. 39 (1963) 3209–3213.

[39] G.V. Candler, R.W. MacCormack, Computation of weakly ionized hypersonic flows in thermochemical nonequilibrium, J. Thermophys. Heat Transf. 5 (1991) 266–273.

[40] M. Di Renzo, L. Fu, J. Urzay, HTR solver: an open-source exascale-oriented task-based multi-gpu high-order code for hypersonic aerothermodynamics, Comput. Phys. Commun. 255 (2020) 107262.

[41] J. Urzay, M. Di Renzo, Engineering Aspects of Hypersonic Turbulent Flows at Suborbital Enthalpies, Annual Research Briefs, Center for Turbulence Research, Stanford University, 2020, pp. 7–32.

[42] C.T. Williams, M. Di Renzo, J. Urzay, Two-Temperature Extension of the Htr Solver for Hypersonic Turbulent Flows in Thermochemical Nonequilibrium, Annual Research Briefs, Center for Turbulence Research, Stanford University, 2021, pp. 95–107.

[43] C.T. Williams, M. Di Renzo, P. Moin, Computational Framework for Direct Numerical Simulation of Shock- Turbulence Interaction in Thermochemical Nonequilibrium, Annual Research Briefs, Center for Turbulence Research, Stanford University, 2022, pp. 203–216.

[44] L. Fu, X.Y. Hu, N.A. Adams, A family of high-order targeted eno schemes for compressible-fluid simulations, J. Comput. Phys. 305 (2016) 333–359.

[45] M. Di Renzo, S. Pirozzoli, Htr-1.2 solver: hypersonic task-based research solver version 1.2, Comput. Phys. Commun. 261 (2021) 107733.

[46] C.-W. Shu, S. Osher, Efficient implementation of essentially non-oscillatory shock-capturing schemes, ii, J. Comput. Phys. 83 (1989) 32–78.

[47] K. Mahesh, S.K. Lele, P. Moin, The influence of entropy fluctuations on the interaction of turbulence with a shock wave, J. Fluid Mech. 334 (1997) 353–379.

[48] S. Lee, S.K. Lele, P. Moin, Interaction of isotropic turbulence with shock waves: effect of shock strength, J. Fluid Mech. 340 (1997) 225–247.

[49] J. Larsson, S.K. Lele, Direct numerical simulation of canonical shock/turbulence interaction, Phys. Fluids 21 (2009) 126101.

[50] C. Huete, A. Cuadra, M. Vera, J. Urzay, Thermochemical effects on hypersonic shock waves interacting with weak turbulence, Phys. Fluids 33 (2021) 086111.

[51] J. Urzay, Supersonic combustion in air-breathing propulsion systems for hypersonic flight, Annu. Rev. Fluid Mech. 50 (2018) 593–627.

[52] T. Passot, A. Pouquet, Numerical simulation of compressible homogeneous flows in the turbulent regime, J. Fluid Mech. 181 (1987) 441–466.

[53] M. Bassenne, J. Urzay, G.I. Park, P. Moin, Constant-energetics physical-space forcing methods for improved convergence to homogeneous-isotropic turbulence with application to particle-laden flows, Phys. Fluids 28 (2016) 035114.

[54] J.B. Freund, Proposed inflow/outflow boundary condition for direct computation of aerodynamic sound, AIAA J. 35 (1997) 740–742.